

# The Molecular Condensations Ahead of Herbig-Haro Objects. III. Radiative and dynamical perturbations of the HH 2 condensation.

Josep Miquel Girart<sup>1,2,3</sup>, Serena Viti<sup>4</sup>, Robert Estalella<sup>3</sup>, David A. Williams<sup>4</sup>

<sup>1</sup> Institut de Ciències de l'Espai (CSIC), Gran Capità 2, 08034 Barcelona, Catalunya, Spain

<sup>2</sup> Institut d'Estudis Espacials de Catalunya

<sup>3</sup> Departament d'Astronomia i Meteorologia, Universitat de Barcelona, Av. Diagonal 647, 08028 Barcelona, Catalunya, Spain

<sup>4</sup> Department of Physics and Astronomy, University College London, London, WC1E 6BT, England, UK

Received ...; accepted ...

## Abstract.

We have carried out an extensive observational study (from BIMA data) and made a preliminary theoretical investigation of the molecular gas around HH 2. The molecular maps show a very complex morphological, kinematical and chemical structure. For clarity we divided the observed region in four subregions: (1) The Ahead Core, located ahead of HH 2: its chemistry may be a consequence of a weak UV field originating in HH 2. The chemical structure within the Ahead Core suggests that it is not homogeneous but probably composed of small clumps; (2) The SO<sub>2</sub> Clump, which is a molecular component within the Ahead Core that is more exposed to the UV radiation from HH 2. An increase of density and relative molecular abundances is observed towards HH 2. The UV radiation is possibly the source of molecular enhancement. Our chemical analysis confirms that this clump must have substructure within it; (3) the West Core, which is surrounded by a ring structure of shocked ionized gas and mid-IR emission. The ring structure is likely a consequence of the fact that the core is in the foreground with respect to the shocked and hot component. The chemistry of this core can be best explained as arising from a combination of an old photo-processed dense clump and a PDR, with or without a warm interface created in the interaction of the outflow with the core; (4) The High Velocity Region, associated with HH 2, is traced by HCO<sup>+</sup> but not by other molecular shock tracers. The chemistry can be accounted for by the interaction of the VLA 1 outflow with a dense clump *via* non-dissociative shocks and by the presence of a very strong UV field. The overall main conclusion of this work confirms the findings of Paper I and II, by demonstrating that in addition to the strong photochemical effects caused by penetration of the UV photons from HH 2 into molecular cloud, a range of complex radiative and dynamical interactions occur. Thus, despite the apparent 'quiescent' nature of the molecular cloud ahead of HH 2, the kinematical properties observed within the field of view suggest that it is possibly being driven out by the powerful winds from the VLA 1 protostar.

**Key words.** ISM: individual: HH 2 — ISM: abundances — ISM: clouds — ISM: molecules — Radio lines: ISM — Stars: formation

## 1. Introduction

Very powerful winds are associated with the earliest stages of star formation. These winds alter significantly the dense molecular environments that surround the protostars. There are two kinds of interaction between the winds with the dense molecular environment; one is dynamic, and the other radiative. The molecular outflows are the main signpost of the dynamical interaction (e. g., Richer et al. 2000). The radiation generated in the strong shocks produced in the Herbig-Haro (HH) objects, as well

as the shock themselves alter the chemical composition of the molecular gas through mantle desorption and gas phase endothermic reactions (e. g., Girart et al. 1994, 2002; Flower et al. 1996; Amin 2001). Thus, it is clear that high angular and spectral resolution maps of the molecular gas where this interaction takes place are very important in order to understand better the interaction mechanism and the properties of both the outflow and of the molecular clouds.

HH 2 is a well studied bright, high excitation HH object, which generates strong UV radiation (e. g., Böhm et al. 1992; Raymond et al. 1997) and presents a very com-

**Table 1.** Frequency setups of the BIMA observations

Frequency (GHz) LSB – USB	Main molecular transitions observed	Dates	System Temperatures
72.2 – 75.8	DCO <sup>+</sup> 1–0, SO <sub>2</sub> 6 <sub>0,6</sub> –5 <sub>1,5</sub> , DCN 1–0, CH <sub>3</sub> SH 3 <sub>0</sub> –2 <sub>0</sub> A <sup>+</sup>	2000 Nov, 2001 Mar	250–1000 K
72.7 – 76.4	H <sub>2</sub> CO 1 <sub>0,1</sub> –0 <sub>0,0</sub> , SO <sub>2</sub> 6 <sub>0,6</sub> –5 <sub>1,5</sub> , DCN 1–0	2000 Apr	300– 850 K
85.3 – 89.0	HCN 1–0, HCO <sup>+</sup> 1–0, H <sup>13</sup> CO <sup>+</sup> 1–0, C <sub>3</sub> H <sub>2</sub> 2 <sub>1,2</sub> –1 <sub>0,1</sub> , HCS <sup>+</sup> 2–1	2000 Apr	200– 600 K
86.1 – 90.0	SO 2 <sub>2</sub> –1 <sub>1</sub> , HCOOH 4 <sub>0,4</sub> –3 <sub>0,3</sub>	2000 Jul	200– 500 K
86.7 – 89.7	H <sup>13</sup> CO <sup>+</sup> 1–0, H <sup>13</sup> CN 1–0, SiO 2–1	2003 May, Jun <sup>a</sup>	170– 600 K
96.7 –100.0	CH <sub>3</sub> OH 2 <sub><i>n</i></sub> –1 <sub><i>n</i></sub> , HC <sub>3</sub> N 11–10	1999 Oct	200– 500 K
98.0 –101.0	CS 2–1, OCS 8–7	1999 Dec, 2000 May	200– 800 K
99.3 –103.0	SO 3 <sub>2</sub> –2 <sub>1</sub> , H <sub>2</sub> CS 3 <sub>0,3</sub> –2 <sub>0,2</sub>	2000 Jul	300–1400 K
100.5 –104.1	SO <sub>2</sub> 3 <sub>1,3</sub> –2 <sub>0,2</sub> , NH <sub>2</sub> CN 5 <sub>1,4</sub> –4 <sub>1,3</sub>	2000 Nov, 2001 Mar, May	140– 400 K
104.2 –107.8	SO <sub>2</sub> 3 <sub>1,3</sub> –2 <sub>0,2</sub>	2000 Jul	300– 800 K
109.7 –113.0	SO 2 <sub>3</sub> –1 <sub>2</sub> , C <sup>18</sup> O 1–0, CN 1–0	2000 Apr, May	280–1300 K
109.9 –113.4	C <sup>18</sup> O 1–0, <sup>13</sup> CO 1–0, CN 1–0, CH <sub>3</sub> CN 6 <sub><i>n</i></sub> –5 <sub><i>n</i></sub> , HNC O 5 <sub>0,5</sub> –4 <sub>0,4</sub>	2000 Nov, 2001 Mar–May	350–1100 K

<sup>a</sup> 2003 June observations were carried out in the D configuration

plex morphology (Hester et al. 1998; Bally et al. 2002). It is driven by HH 1–2 VLA 1 (hereafter VLA 1), a Class 0 protostar (André, Ward–Thompson & Barsony 2000). HH 2 is also associated with CO emission from the VLA 1 molecular outflow (Moro–Martín et al. 1999). A dense cloud of molecular gas and dust, apparently quiescent, appears ahead of HH 2 (Davis, Dent & Bell Burnell 1990; Torrelles et al. 1992; Dent, Furuya & Davis 2003).

Girart et al. (2002; hereafter Paper I) carried out a molecular line survey in the 0.8–4.0 mm range and at an angular resolution of  $\sim 30''$  of the dense molecular gas ahead of HH 2. From these observations we derive a temperature of  $\sim 13$  K and a density of  $3 \times 10^5$  cm<sup>-3</sup>. The observations show a characteristic chemistry that can be accounted for with chemical models of irradiated clumps (e. g., Taylor & Williams 1996; Viti & Williams 1999); the models indicate that photochemistry induced by HH radiation in regions that have not yet been shocked should produce a characteristic chemistry that is a signature of that origin. A detailed modeling of the conditions of the molecular clump ahead of HH 2 was carried out by Viti et al. (2003; hereafter Paper II). From the chemical analysis of this work we found that the ‘illuminated’ clump was young when it was first irradiated by HH 2 and that to account for the observed column densities a density gradient is required (i. e., the clump does not have a uniform density). In addition, we found that the peculiar chemistry will last for no more than a few hundred years, since the UV radiation will ultimately destroy the molecular content. The chemical effects, however, last longer as the relevant region ‘eats’ into the core.

In Paper I we studied the observational properties and the molecular gas at an angular resolution of  $30''$  at one position ahead of HH 2, by using data from the CSO and BIMA. In Paper II we carried out chemical analysis by using the results of Paper I. The aim of this work is to study in detail, at higher angular resolution ( $\sim 10''$ ), the

distribution and properties of the molecular gas around HH 2 and to understand how the powerful outflow arising from VLA 1 affects its properties. In § 2 we summarize the observational parameters of the maps. In § 3 we describe the morphological properties of the molecular emission. In § 4 we analyze the data. In § 5 we discuss the chemical as well as the physical properties of the molecular environment around HH 2 and we consider why the regions observed appear to be chemically distinct. A brief summary and the conclusions are given in § 6.

## 2. Observations

The observations were carried out with the 10–antenna BIMA array<sup>1</sup> at the Hat Creek Radio Observatory. The phase calibrators used were QSOs 0541–056, 0607–085 and 0609–157. Absolute flux calibration was checked by observing Saturn or Mars. A total of 12 frequency setups were used, which covered frequencies between 72.0 and 113.5 GHz. All the frequency setups were observed in the C configuration (i. e., antenna separation from 6.3 to 100 m). At 3 mm this configuration provides a visibility coverage between 20 and 300 nanoseconds, i. e., an angular resolution of  $\sim 9''$ . Table 1 shows for each frequency setup, the frequencies of the lower and upper side band (LSB and USB), the main molecular transitions observed, the observation dates and the range of system temperatures achieved. The digital correlator was configured to sample part of the 800 MHz wide IF passband in several windows, with adjustable frequency resolution. The typical window for the line observations was configured with a 25 MHz bandwidth and 256 channels, giving a spectral resolution of 97.7 kHz. Thus, with the powerful correlator we were able to observe many molecular transitions.

<sup>1</sup> The BIMA array is operated by the Berkeley–Illinois–Maryland Association with support from the National Science Foundation.

**Table 2.** Parameters of the BIMA maps

Molecule Transition	$\nu$ (GHz)	Synthesized Beam HPBW, PA (arcsec, deg)	$\Delta v$ (km s <sup>-1</sup> )	<i>rms</i> (Jy/ beam)
DCO <sup>+</sup> 1-0	72.0393	19.3×7.3, 1	0.20	0.30
H <sub>2</sub> CO 1 <sub>0,1</sub> -0 <sub>0,0</sub>	72.8380	18.0×9.4, 15	0.20	0.27
C <sub>3</sub> H <sub>2</sub> 2 <sub>1,2</sub> -1 <sub>0,1</sub>	85.3389	14.1×7.1, -1	0.34	0.10
SO 2 <sub>2</sub> -1 <sub>1</sub>	86.0934	12.9×7.6, 0	0.34	0.16
H <sup>13</sup> CN 1-0	86.3402	17.6×11.8, 4	0.33	0.11
H <sup>13</sup> CO <sup>+</sup> 1-0	86.7543	17.4×11.2, 9	0.33	0.11
SiO 2-1	86.8470	17.7×11.7, 6	0.33	0.11
HCN 1-0	88.6318 <sup>a</sup>	12.7×7.1, 0	0.33	0.10
HCO <sup>+</sup> 1-0	89.1885	13.2×7.0, 1	0.33	0.11
CH <sub>3</sub> OH 2 <sub>n</sub> -1 <sub>n</sub>	96.7414 <sup>b</sup>	11.7×6.4, 4	0.30	0.13
CS 2-1	97.9810	14.2×6.1, 10	0.30	0.14
SO 3 <sub>2</sub> -2 <sub>1</sub>	99.2999	11.9×6.6, 15	0.59	0.14
SO <sub>2</sub> 3 <sub>1,3</sub> -2 <sub>0,2</sub>	104.0294	9.9×5.6, 1	0.28	0.05
SO 2 <sub>3</sub> -1 <sub>2</sub>	109.2522	10.4×5.9, 2	0.27	0.15
C <sup>18</sup> O 1-0	109.7822	10.1×5.9, 1	0.27	0.12
<sup>13</sup> CO 1-0	110.2014	9.7×6.3, -8	0.27	0.13
CN 1-0	113.4910 <sup>c</sup>	12.0×8.9, -5	0.52	0.08

<sup>a</sup> Frequency for the F=2-1 hyperfine line. Observations also detected the F=1-1 and F=0-1 hyperfine lines

<sup>b</sup> Frequency for the 2<sub>0</sub>-1<sub>0</sub>A<sup>+</sup> line. Observations also detected the 2<sub>-1</sub>-1<sub>-1</sub> E line

<sup>c</sup> Frequency for the 1-0  $\frac{3}{2}, \frac{5}{2}-\frac{1}{2}, \frac{3}{2}$  line. Observations also detected the  $\frac{3}{2}, \frac{1}{2}-\frac{1}{2}, \frac{1}{2}$  and  $\frac{1}{2}, \frac{3}{2}-\frac{1}{2}, \frac{3}{2}$  lines. The maps were obtained by applying a Gaussian taper of 26 k $\lambda$  to the visibilities.

Table 2 from Paper I gives the list of the lines observed before 2003, with the peak intensity or upper limits for an angular resolution of 30". In the 2003 observations, of the three lines observed (see Table 1), we only detected the H<sup>13</sup>CO<sup>+</sup> 1-0.

The phase center of the observations was  $\alpha(J2000) = 5^{\text{h}}36^{\text{m}}27^{\text{s}}.20$ ;  $\delta(J2000) = -6^{\circ}47'27''$ . The FWHM BIMA primary beam ranges from 2'.7 at 72 GHz to 1'.7 at 113 GHz, and thus our observations engulfs within the primary beam the HH 2 object and dense core associated with it. For the 109.9–113.4 GHz (LSB–USB) frequency setup, the observations (which included the <sup>13</sup>CO, C<sup>18</sup>O and the CN lines) were done with a mosaic of five points: a field centered in the phase center, and the other fields located 48" N, S, E and W of the the phase center. The data were calibrated using the MIRIAD software. Maps were made with the (*u*, *v*) data weighted by the associated system temperatures and using natural weighting. Table 2 lists all the molecular lines detected from the observations listed in Paper I as well as the three lines observed in 2003. The table includes the channel resolution, the resulting synthesized beam and the *rms* noise of the maps at this channel resolution.

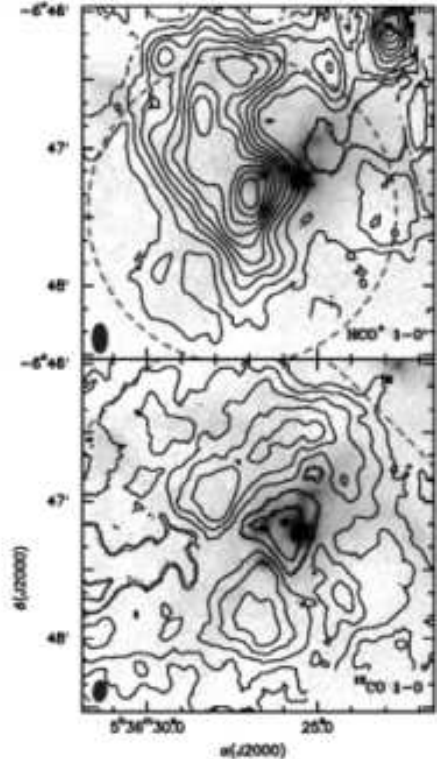


**Fig. 4.** Superposition of the [SII] image (from Curiel, private communication) and the BIMA contour maps of the zero-order moment (integrated emission over the 5.3 to 11.3 km s<sup>-1</sup> velocity range) of the HCO<sup>+</sup> 1-0 and <sup>13</sup>CO 1-0 around HH 2. The BIMA maps are corrected by the primary beam response. Contours are 1, 2.5, 4, ..., 32.5 times 0.45 (HCO<sup>+</sup>) and 0.72 (<sup>13</sup>CO) Jy km s<sup>-1</sup>. The contours with dots around HH 2 indicates an emission valley. The dashed thick line shows the BIMA beam response at the 0.5 level with respect to phase center. The synthesized beam is shown in the bottom left corner of the panels. The position of the driving source of the HH 1-2 outflow (VLA 1) is shown as a filled square in the upper-right corner of the panels.

### 3. Results

Figures 1, 2 and 3 show the channel maps over the 6 to 10 km s<sup>-1</sup> velocity range of the molecular transitions with emission detected at least in one channel. For most of the molecules detected their emission is comprised within this velocity range. Figure 4 shows the zero-order moment of the emission for the <sup>13</sup>CO and HCO<sup>+</sup> 1-0 lines. The kinematical and morphological complexity of this region is clear from these figures.

For clarity, we will divide the observed region in four subregions taking into account the properties of the dif-

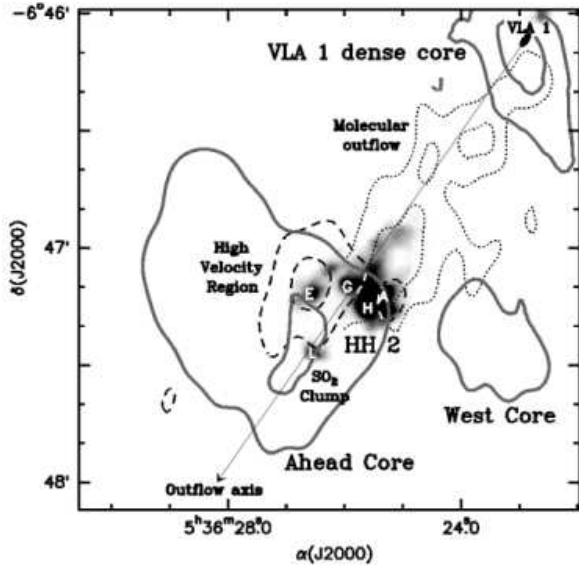


**Fig. 5.** Sketch of the HH 2 region. Thick grey contours show the main molecular regions (the Ahead and West Cores with respect to HH 2 and the VLA 1 dense core). The dashed contours show the high velocity  $\text{HCO}^+$  clump. The dotted points contours show the jet-like molecular outflow (obtained from the  $\text{HCO}^+$  emission at a  $v_{\text{LSR}}$  velocity of  $7.3 \text{ km s}^{-1}$  after masking the contribution from the Ahead Core). The grey scale shows the  $[\text{SII}]$  emission (from Curiel, private communication). The white labels within the  $[\text{SII}]$  emission indicates the HH 2 knot names. The small filled ellipsoid shows the position and elongation direction of the VLA 1 radio jet, the powering source of the HH 1–2 outflow. The arrow shows the direction of the outflow.

ferent molecular species detected and the properties of other tracers detected at other wavelengths (see Figure 5): (1) The molecular core ahead of HH 2 (hereafter Ahead Core); this region includes the region studied in Paper I and II, which coincides with the compact emission traced by SO and  $\text{SO}_2$ ; (2) The molecular core west of HH 2 (hereafter West Core); (3) The high velocity molecular emission spatially associated with HH 2 (hereafter High Velocity Region); (4) The dense core surrounding the HH 2 driving source, VLA 1. In the following three subsections we describe the first three regions. The VLA 1 dense core is detected clearly in several molecules ( $^{13}\text{CO}$ ,  $\text{H}^{13}\text{CO}^+$ ,  $\text{H}_2\text{CO}$ , HCN,  $\text{C}_3\text{H}_2$ ) in the  $10 \text{ km s}^{-1}$  channel map (see Figs. 1, 2 and 3). However, since it is located far from the phase center of the BIMA observations ( $\sim 1.7$ ) we do not study its properties. The properties of this core have been well described in previous studies (e. g., Torrelles et al. 1994; Choi & Zhou 1997). Thus, below we describe the first three regions. We also describe the overall kinematics of the dense gas seen within the field of view. In the last

subsection of the results we briefly describe the emission traced by the  $^{13}\text{CO}$  1–0.

### 3.1. The Ahead Core

We define the Ahead Core as the cold dense molecular and dust component located ahead of HH 2; it was first detected from observations of  $\text{HCO}^+$  (Davis et al. 1990) and  $\text{NH}_3$  (Torrelles et al. 1992, 1994). Dent et al. (2003) have recently studied the submm dust emission from the Ahead Core, which arises from a region with a size of  $0.13 \times 0.09 \text{ pc}^2$ . From the dust properties, Dent et al. (2003) derive a total mass for the core of  $3.8 M_{\odot}$ , an averaged dust temperature of 22 K and a core luminosity of  $13 L_{\odot}$ .

For some species (e. g.,  $\text{HCO}^+$ ; see Fig. 4), the maps of their integrated emission over all the velocity range where the emission is detected (excluding the high velocity component) show that the Ahead Core is not an isolated molecular structure but it is connected with the VLA 1 dense core. Indeed and despite the BIMA primary beam attenuation, the overall morphology of the  $\text{HCO}^+$  1–0 agrees well with that from the  $\text{HCO}^+$  3–2 integrated emission (Choi & Zhou 1997). However, we consider the Ahead Core as the molecular emission that is spatially coincident with the submm dust structure detected ahead of HH 2 (see Figure 2 of Dent et al. 2003). The emission associated with the Ahead Core emits in the  $5.2\text{--}7.8 \text{ km s}^{-1}$   $v_{\text{LSR}}$  range. Figure 6 shows the averaged emission within this velocity range for some of the molecular transitions presented in this paper as well as  $\text{NH}_3$  (1,1) from Torrelles et al. (1994), and the 0.85 mm dust map from Dent et al. (2003).

The emission of the Ahead Core is traced by all the detected lines in this work, except for the  $\text{C}_3\text{H}_2$   $2_{1,2}\text{--}1_{0,1}$  line (which is only detected towards the VLA 1 dense core), as can be seen in the 6, 7 and  $8 \text{ km s}^{-1}$  channel maps of Figures 1, 2 and 3. Despite the apparent complexity of the molecular emission for the different species, we can group them according to their morphologies within the Ahead Core.

First,  $\text{HCO}^+$  and isotopes, as well as HCN and  $\text{H}_2\text{CO}$  are the only species that trace the whole dusty structure from the Ahead Core. In particular, Fig. 6 shows that there is a good spatial correspondence of these species with the submm dust emission.  $\text{NH}_3$  can also be included in this group, since its emission also follows most of the dust emission (Fig. 6), especially if compared with the molecular emission from species of other groups (see below). In spite of the overall agreement between the emission of these molecules and the dust, the intensity peak of the molecular emission is located around HH 2 knot L (only  $\text{HCO}^+$  peak coincides with that of the dust).  $\text{HCO}^+$  is the only molecule that has emission engulfing most of HH 2, including the brightest and highest excitation knots, H and A, where no dust is detected.

A second group of molecules comprise SO,  $\text{SO}_2$  and  $\text{CH}_3\text{OH}$ : they appear to be significantly more compact

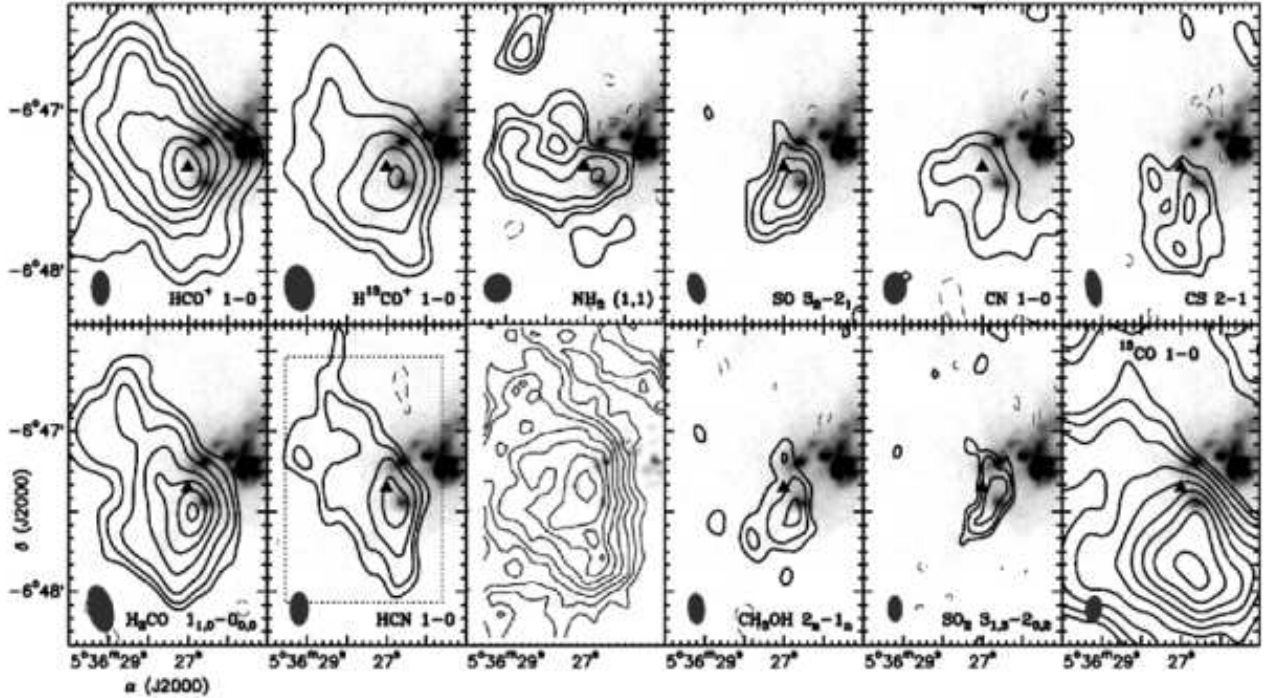


**Fig. 6.** Contour maps of the ahead core for the dust emission at 0.85 mm (adapted from Figure 2 of Dent et al. 2003) and for several molecular lines. The grey scale [SII] image (from Curiel, private communication) is also shown in the molecular line panels. The molecular maps shown here are obtained by averaging the emission over the 5.2 to 7.8  $\text{km s}^{-1}$   $v_{\text{LSR}}$  velocity range. The  $\text{NH}_3$  (1,1) map was obtained from the data of Torrelles et al. (1994). The triangle shows the position of the 0.85 mm dust emission peak. The dotted rectangle in the HCN panel shows the area used to compute the molecular abundances in the Ahead Core.

than the previous species (and the dust) and their emission is located ahead of the brightest HH 2 knots and with the strongest emission spatially coincident with HH 2 knot L (Fig. 6). Interestingly, the emission of  $\text{CH}_3\text{OH}$ ,  $\text{SO}$  and  $\text{SO}_2$  appears displaced to the west with respect to dust peak, i. e., apparently, they trace the face of the dust core exposed to the HH 2 object (see Fig. 6).

A third group includes CS and the CO isotopes. The CS and  $\text{C}^{18}\text{O}$  emission and the bulk of the  $^{13}\text{CO}$  emission from the Ahead Core arise south of the HH 2 knot L, with little or no emission in the east part of the Ahead Core. The peaks of emission of these molecules are located 15'' to 30'' south of the dust peak and are roughly coincident with secondary dust peaks.

Finally, the CN emission has an inverted ‘L’ morphology centered and peaking at the same position as the dust. To the south of the dust peak it follows approximately the CS emission.

### 3.2. The West Core

The West Core is the molecular structure detected west of HH 2 at the 6  $\text{km s}^{-1}$  channel of Figs. 1, 2 and 3. This core is also traced by the dust at submm wavelengths

(Dent et al. 2003). Interestingly, very recent mid-IR observations shows that this molecular clump is surrounded by a ring structure of hot dust (Lefloch et al. 2005). This hot ring shows also PAH emission (Lefloch et al. 2005),  $\text{H}\alpha$  (Warren-Smith & Scarrott 1999) and [SII] (Fig. 7).

The West Core is detected in  $\text{HCO}^+$ ,  $^{13}\text{CO}$ ,  $\text{C}^{18}\text{O}$ ,  $\text{H}_2\text{CO}$ , CN, HCN, CS and marginally also in  $\text{SO}_2$  and  $\text{C}_3\text{H}_2$ . This core is not detected in  $\text{NH}_3$  (Torrelles et al. 1994). Figure 7 shows clearly how well the [SII] surrounds the molecular emission. The [SII] hole, where the molecular emission appears, is remarkably circular with a diameter of  $\sim 30''$  or 0.06 pc. The [SII] hole is especially well traced by the CO isotopes, whereas the CN and  $\text{HCO}^+$  are slightly shifted to the north with respect to the center of this hole. The molecular line widths are quite narrow ( $\Delta v \simeq 0.4 \text{ km s}^{-1}$ ) and centered at  $v_{\text{LSR}}$  of 6.3  $\text{km s}^{-1}$ . A weaker and broader component is also detected at  $v_{\text{LSR}} = 8.8 \text{ km s}^{-1}$ .

### 3.3. High Velocity Region

Similarly to Dent et al. (2003), we found broad  $\text{HCO}^+$  1-0 emission ( $v_{\text{LSR}}$  ranging from  $-8$  to 24  $\text{km s}^{-1}$ ) spatially compact and associated with HH 2. Figure 8 shows clearly

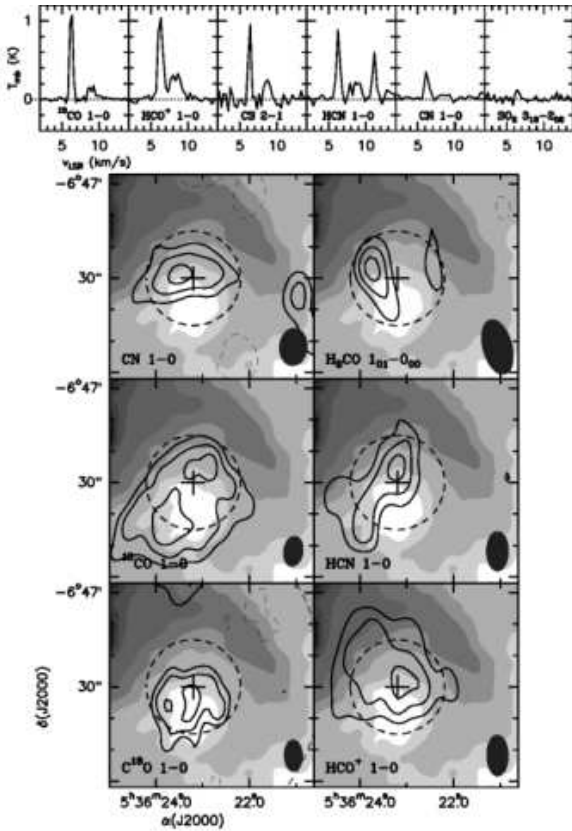


**Fig. 7.** *Bottom panels:* Superposition of the grey scale [SII] image (from Curiel, private communication) and the  $^{13}\text{CO}$ ,  $\text{HCO}^+$ ,  $\text{H}_2\text{CO}$ ,  $\text{C}^{18}\text{O}$ ,  $\text{CN}$  and  $\text{HCN}$  BIMA contour maps at the  $6 \text{ km s}^{-1}$  velocity channel of the molecular clump west of HH 2. The [SII] image was convolved with a Gaussian with a FWHM of  $4''$  in order to enhance the weak ring structure around the molecular emission. Contours are 50, 70 and 90% of the peak. The cross shows the position of the submm dust position shown in Figure 2 of Dent et al. (2003). The synthesized beam of the molecular maps are shown in the bottom right corner. The dashed circle shows the area used to estimate the column densities (see § 4.2). *Top panels:* Primary beam corrected spectra of the molecular lines (shown in the bottom right of the panels) taken at  $\alpha(J2000) = 5^{\text{h}}36^{\text{m}}23^{\text{s}}.2$ ;  $\delta(J2000) = -6^{\circ}47'30''$  and at an angular resolution of  $30''$ . For the  $\text{CN}$  the transition shown is the  $N=1-0 \ J=3/2-1/2 \ F=5/2-3/2$ . The  $^{13}\text{CO}$  and  $\text{HCO}^+$  line intensities have been scaled down a factor 3 and 2, respectively.

that the high velocity  $\text{HCO}^+$  emission is well correlated with the shock-excited near-IR  $1-0 \ \text{S}(1)\text{H}_2$  emission. The spatial correlation is even better with respect to the  $\text{H}_2 \ 0-0 \ \text{S}(2)$  line (see Fig. 1 from Lefloch et al. 2003): The strongest high velocity  $\text{HCO}^+$  emission appears located around the HH 2 knot E and there is also weaker emission near the highest excitation HH 2 knots. A more detailed

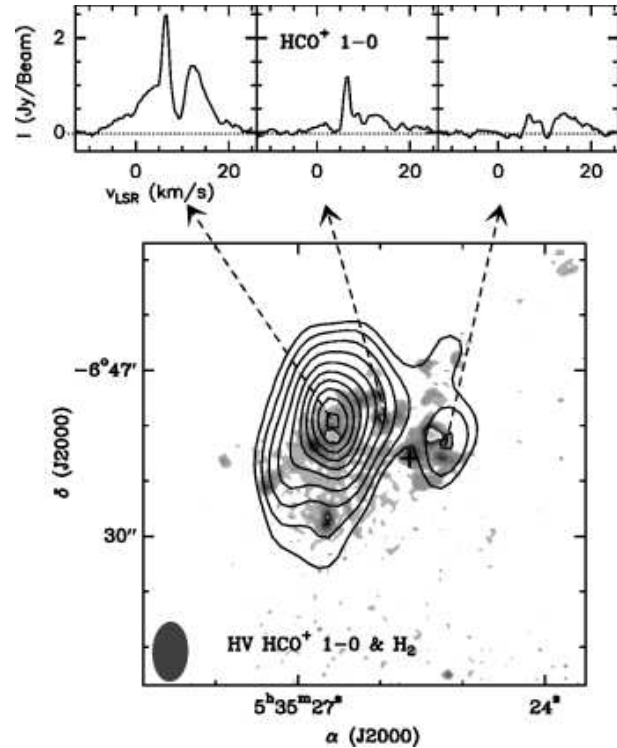


**Fig. 8.** *Bottom panels:* Superposition of the grey scale near-IR  $\text{H}_2 \ 1-0 \ \text{S}(1)$  image ( $K'$  band; Curiel, private communication) and the contour map of the integrated high velocity  $\text{HCO}^+$  emission over the  $-5$  to  $5$  and  $11$  to  $21 \text{ km s}^{-1}$   $v_{\text{LSR}}$  interval, respectively.  $\text{HCO}^+$  contours levels are 3, 5, 8, 12, 17, 22, 27, 32, 37 and 42 times the  $rms$  noise of the map,  $0.2 \text{ Jy km s}^{-1}$ . The synthesized beam is shown in the bottom left corner of each panel. *Top panel:*  $\text{HCO}^+$   $1-0$  spectra of the high velocity gas. The cross marks the position of the X-ray source (Pravdo et al. 2001).

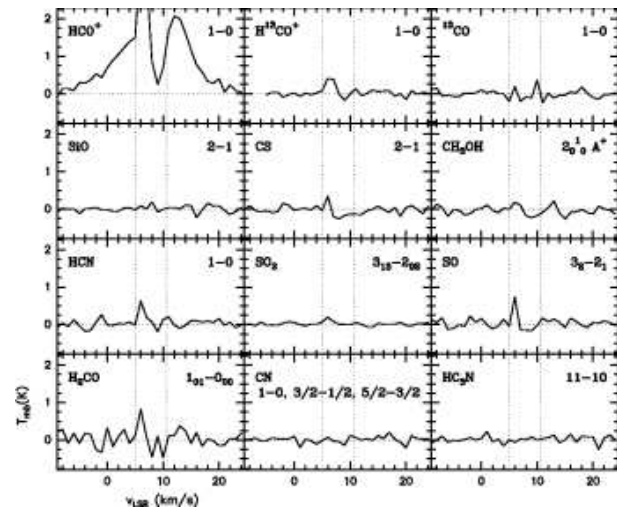


**Fig. 9.** Spectra of the different molecular transitions at the intensity peak of the high velocity  $\text{HCO}^+$   $1-0$  emission ( $\alpha(J2000) = 5^{\text{h}}36^{\text{m}}26^{\text{s}}.57$ ;  $\delta(J2000) = -6^{\circ}47'9''.1$ ).

description of the high velocity  $\text{HCO}^+$  around HH 2 and its properties is given by Dent et al. (2003).

As shown in Figure 9, and from our BIMA data, the high velocity emission associated with HH 2 is detected only in the  $\text{HCO}^+$  1–0 line (the only other reported molecule with high-velocity emission is CO: e. g., Moro–Martín et al. 1999). This is interesting, since species that are usually strongly enhanced in shocked molecular clumps, such as SiO, CS,  $\text{CH}_3\text{OH}$ ,  $\text{H}_2\text{CO}$  and SO (e. g., L1157: Bachiller & Pérez Gutiérrez 1997) are not detected in this region.

### 3.4. The overall kinematics of the dense gas

A look at the channel maps of the  $\text{HCO}^+$  emission (Fig. 1) shows that there is a clear velocity gradient in the dense molecular structure connecting the Ahead Core with the VLA 1 dense core. That is, the emission closer to the systemic velocity ( $v_{\text{LSR}} \simeq 9.5 \text{ km s}^{-1}$ , Moro–Martín et al. 1999) appears located closer to the VLA 1 dense core, whereas the emission with bluer velocities appears located closer to the Ahead Core. This is also observed in the emission of other molecules but with a weaker signal-to-noise ratio (e. g., HCN and  $\text{H}_2\text{CO}$ ). Note that the emission from this molecular structure from the 9 and 10  $\text{km s}^{-1}$  velocity channels of Figures 1, 2 and 3 is different for the different molecules. Since this is the systemic velocity, these differences could be due to high optical depths, or to other factors, such a different excitation or chemical conditions. We will not discuss further these differences and we will discuss only the kinematics from the  $\text{HCO}^+$  and  $\text{H}^{13}\text{CO}^+$ .

The velocity gradient is also clearly shown in the first-order moment map of the  $\text{HCO}^+$  (Fig. 10). The most blueshifted velocities,  $v_{\text{LSR}} \sim 6.4 \text{ km s}^{-1}$ , appear close to HH 2 knot L in the Ahead Core, and in the West Core. South of the Ahead Core the velocity of the gas goes back to the systemic velocity.

The second-order moment map of the  $\text{HCO}^+$  (Fig. 10) shows that most of the emission has a line width (FWHM) in the 0.7–1.6  $\text{km s}^{-1}$  range. The largest line widths are observed around HH 2 knot E, where the high velocity  $\text{HCO}^+$  is observed. Large line widths are also observed along three arms emerging around knot E: one connecting with VLA 1 and coinciding with the outflow axis and the other two perpendicular to this one. This region of line width enhancement form a rotated ‘T-like’ shape.

In order to see better the overall kinematics and, in particular, the region of line width enhancement, we show in Figure 11 the position–velocity maps for the  $\text{HCO}^+$  and  $\text{H}^{13}\text{CO}^+$  1–0 along three different cuts. Two of them (cuts 1 and 2) are along the direction of the line widths enhancement (see previous paragraph). The other (cut 3) is parallel to cut 2 but further away from VLA 1 (although still within the Ahead Core).

Despite of the complexity of Figures 10 and 11, the kinematics of the region can be summarized as follows:

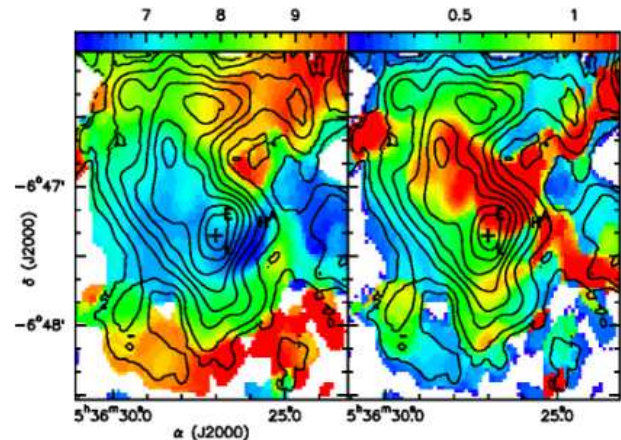


**Fig. 10.** Superposition of the the BIMA contour maps of the zero-order moment (integrated emission) with the false-color image of first-order (bottom panel) and second-order (top panel) maps of the  $\text{HCO}^+$  1–0. The moment maps were obtained in the 5.35–11.26  $\text{km s}^{-1}$   $v_{\text{LSR}}$  range. The cross shows the position of the 0.85 mm dust emission peak. The labels indicate the HH 2 knot names.

- The region around HH 2 knot E shows the largest line widths because of the contribution from the high velocity  $\text{HCO}^+$  (this corresponds to the 0'' offset position in the 1 and 2 cuts of Fig.11).
- One of the regions of line width enhancement (the one connecting VLA 1 with HH 2) is spatially coincident with the molecular outflow associated with HH 2. The  $\text{HCO}^+$  emission presents a double peak along the molecular outflow axis (negative offset positions in cut 1 of Fig. 11). The emission from the more blueshifted peak arise from a collimated structure connecting VLA 1 with the Ahead Core (see Fig. 5 and the 7  $\text{km s}^{-1}$  channel of the  $\text{HCO}^+$  of Fig. 1). Interestingly, the CO emission from the molecular outflow in this region is mainly redshifted with respect to the systemic velocity (see Moro–Martín et al. 1999), which is the reverse situation of the  $\text{HCO}^+$  emission. Taking into account that the outflow axis is almost on the plane of the sky, this suggests that the  $\text{HCO}^+$  is possibly tracing the surface of interaction of the molecular outflow with the dense molecular gas in the foreground face of the outflow lobe.
- Cut 3 shows that the most blueshifted velocities appear at the intersection of the outflow axis with the Ahead Core (0'' offset position) and the velocity becomes closer to the systemic velocity as the emission gets further away from the outflow axis. The same behavior is seen in the velocity gradient shown by the first-order moment map of Figure 10. Cut 2 shows a similar trend than cut 3 but, in addition, there are two other velocity components that appears only in  $\text{HCO}^+$ , the high velocity component at the 0'' offset position

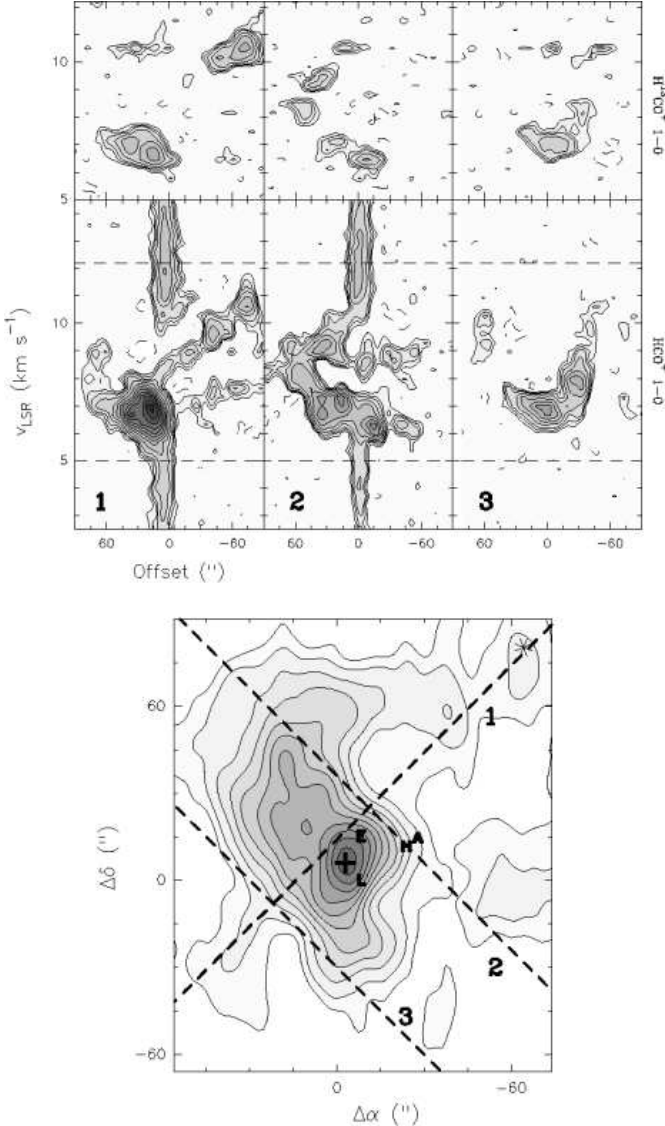


**Fig. 11.** *Bottom panel:* Zero-order moment map of the  $\text{HCO}^+$ . The dashed lines and numbers shows the direction of the position-velocity cuts shown in the upper panels. The cross shows the position of the 0.85 mm dust emission peak. The labels indicates the HH 2 knot names. *Upper panels:* Position-velocity maps of the  $\text{HCO}^+$  and  $\text{H}^{13}\text{CO}^+$  1-0 emission. The origin of position offsets of panels 1 and 2 are the intersection of the dashed lines 1 and 2 in the bottom panel, while for panel 3 is the intersection of dashed lines 1 and 3. The sign of the offsets corresponds to the sign of  $\Delta\alpha$  in the bottom panel.

and a component at  $\sim 8 \text{ km s}^{-1}$ . Since cut 2 follows the border of the Ahead Core facing VLA 1, the latter component may be an indication of interaction of the outflow with the dense core.

### 3.5. The $^{13}\text{CO}$ emission

The  $^{13}\text{CO}$  emission (3 and Fig. 4) shows significantly more structure than the other molecular species, includ-

ing  $\text{HCO}^+$ . This is because of the CO low dipole moment, which allows the molecule to trace low density molecular gas (undetected with the higher density tracers). Fig. 4 shows that within the  $^{13}\text{CO}$  field of view (which is larger than for the other molecules because of the mosaiced observations) the emission spreads out almost everywhere except in a small region spatially coincident with HH 2. The strongest emission surrounds HH 2. It is interesting to note that some of the structures traced by the high density tracers are not well traced or traced significantly differently by the  $^{13}\text{CO}$ .

At the systemic velocities (9 and  $10 \text{ km s}^{-1}$  velocity channel maps of Fig. 3) the strongest  $^{13}\text{CO}$  emission arises from a clear V-shaped structure, with its vertex located near VLA 1, facing and surrounding HH 2. The northern part of this structure corresponds approximately to the high density molecular gas that connects the Ahead Core with the VLA 1 dense core. Given the direction of the outflow (from VLA 1 to HH 2), the V-shaped morphology seems to trace the walls of a cavity created by the HH 1-2 outflow. Indeed, within this cavity and connecting VLA 1 and HH 2 there is a highly collimated molecular outflow (Moro-Martín et al. 1999).

## 4. Analysis

In order to compare properly the different species and derive the temperature and column densities, we first made maps of the different transitions at the same angular resolution. This angular resolution was set to  $15'' \times 9''$ ,  $PA \simeq 0^\circ$ .

### 4.1. The Ahead Core

The physical parameters for the Ahead Core were derived from the maps of the integrated emission within the  $5.2\text{--}7.8 \text{ km s}^{-1}$  velocity range.

#### 4.1.1. Optical depth of the $\text{HCO}^+$ and $\text{HCN}$ 1-0 lines

The  $\text{HCO}^+$  1-0 optical depth was derived from the ratio of the  $\text{H}^{13}\text{CO}^+$  and  $\text{HCO}^+$  integrated emission maps, corrected for the primary beam response. The highest values of the  $\text{HCO}^+$  1-0 optical depth within the FWHM of the primary beam are found south of HH 2, where the optical depth reaches up to  $\sim 20$ . The optical depth smoothly decreases to 2-4 east and northeast of HH 2.

The  $\text{H}^{13}\text{CN}$  1-0 is not detected, so only upper limits can be derived for the  $\text{HCN}$  1-0 optical depth. Since the  $\text{HCN}$  is quite extended, channel maps of both isotopes were smoothed to an angular resolution of  $20''$ . From these maps we estimate that  $\tau_{\text{HCN}} \lesssim 10$ . This implies that the observed  $\text{HCN}$  column density derived in Paper I could be underestimated by a factor of  $\lesssim 10$ . In fact, from Paper II, the best matching model (B15) at  $\sim 100 \text{ yrs}$  gave  $\text{HCN}$  abundances ranging from  $\sim 2 \times 10^{11} \text{ cm}^{-2}$  at 1 mag to  $\sim 6 \times 10^{16} \text{ cm}^{-2}$  at 5 mags; for a 3 mags gas we have a theoretical column density of  $2.7 \times 10^{13}$  which is indeed only



**Table 3.** Mean column densities and abundances in the Ahead Core

Molecule	$N[\text{mol}]$ ( $\text{cm}^{-2}$ )	$X[\text{mol}]^b$
CO <sup>a</sup>	$2.9 \times 10^{17}$	$3.2 \times 10^{-5}$
H <sub>2</sub> CO	$3.0 \times 10^{13}$	$3.4 \times 10^{-9}$
HCO <sup>+</sup>	$2.9 \times 10^{13}$	$3.2 \times 10^{-9}$
CH <sub>3</sub> OH	$1.4 \times 10^{13}$	$1.5 \times 10^{-9}$
SO	$6.7 \times 10^{12}$	$7.4 \times 10^{-10}$
HCN	$1.5 \times 10^{12}$	$1.6 \times 10^{-10}$
SO <sub>2</sub>	$1.2 \times 10^{12}$	$1.3 \times 10^{-10}$
CS	$9.2 \times 10^{11}$	$1.0 \times 10^{-10}$
CN	$6.7 \times 10^{11}$	$7.4 \times 10^{-11}$
DCO <sup>+</sup>	$2.2 \times 10^{11}$	$2.4 \times 10^{-11}$

<sup>a</sup> Here after the CO column densities are derived adopting a <sup>12</sup>CO to <sup>13</sup>CO ratio of 63 (Langer & Penzias 1993).

<sup>b</sup>  $X[\text{mol}]$  is the abundance with respect to H<sub>2</sub>

a factor of 10 higher than the observed column density of  $4 \times 10^{12} \text{ cm}^{-2}$ .

#### 4.1.2. Mean physical parameters

The total mass of the Ahead Core is  $3.8 \pm 0.4 M_{\odot}$ , as derived from submm dust observations (Dent et al. 2003). To estimate the mean column densities and molecular abundances of the observed species over the whole Ahead Core (using the mass derived from the dust), we integrated the emission of the different species within the  $5.2\text{--}7.8 \text{ km s}^{-1}$  velocity range and over a box of  $1'.0 \times 1'.5$  that encompasses the dust emission ahead of HH 2 shown by Dent et al. (2003). The column densities were estimated assuming an excitation temperature of 10 K. Table 3 shows the estimated absolute molecular abundances averaged over the whole Ahead Core. The relative abundances with respect to the CO are a factor  $\sim 2\text{--}10$  lower than the derived from Paper I. Note however that the relative abundances given in Paper I were obtained for a FWHM beam of  $30''$  at the SO peak, whereas the values derived in Table 3 were obtained over a larger region. This difference can be interpreted as arising from chemical gradients within the Ahead Core.

#### 4.1.3. Gradients within the Ahead Core

We computed the excitation temperature of the SO for the  $3_2\text{--}2_1$  and  $2_3\text{--}1_2$  lines. By using these two transitions the excitation temperature can be expressed as:

$$T_{\text{ex}} \simeq -11.7 \left( \log \left( 1.77 \frac{\int I(\text{SO } 2_3 - 1_2) dv}{\int I(\text{SO } 3_2 - 2_1) dv} \right) \right)^{-1} \quad (1)$$

where  $I$  is the line intensity (in K). The resulting excitation temperature map is shown in Figure 12; there is a

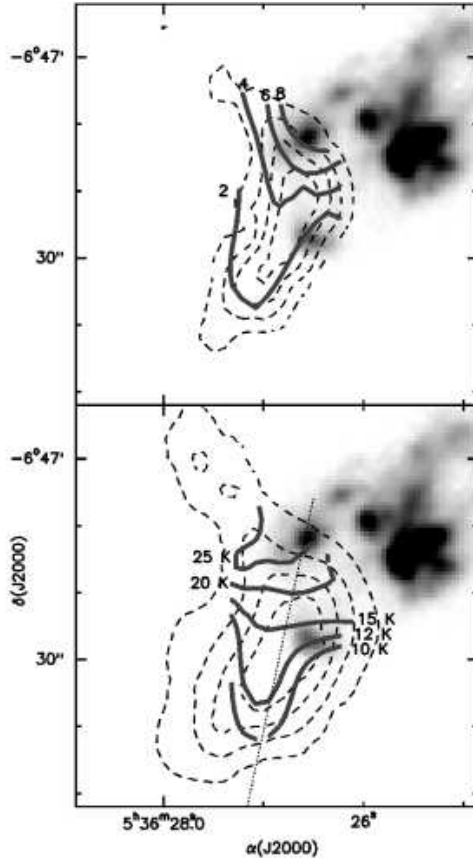


**Fig. 12.** *Top panel:* Superposition of the  $10^{-5} X[\text{SO}_2]/X[\text{CO}]$  map (thick grey contours), the zero-order moment map of the SO<sub>2</sub>  $3_{1,3}\text{--}2_{0,2}$  emission (dashed contours) and [SII] emission (grey scale image). *Bottom panel:* Superposition of the temperature map (thick grey contours) derived from the SO  $2_3\text{--}1_2$  to SO  $3_2\text{--}2_1$  ratio, the zero-order moment map of the SO  $3_2\text{--}2_1$  emission (dashed contours) and the [SII] emission (grey scale image). The dotted line shows the slice done for Figure 13.

gradient, with increasing excitation temperatures towards HH 2.

Column density maps for SO<sub>2</sub> and <sup>13</sup>CO were derived assuming an excitation temperature of 10 K. Figure 12 shows the map of the SO<sub>2</sub> relative abundance with respect to the CO. The map shows a gradient in the SO<sub>2</sub> relative abundance, increasing towards HH 2, having the highest value close to the HH 2 knot E. Note that, if instead of using a constant  $T_{\text{ex}}$ , we use the values derived from the SO line ratio analysis (equation 1) the results do not significantly change.

Given the SO excitation temperature and SO<sub>2</sub> relative abundance gradient towards HH 2 shown in Figure 12, we measured the integrated emission along the direction of this gradient, which approximately coincides with the SO and SO<sub>2</sub> major axis. From these slices we computed: (1) The excitation temperature for the SO  $3_2\text{--}2_1$  and  $2_3\text{--}1_2$  lines (see first paragraph of this section). (2) The column

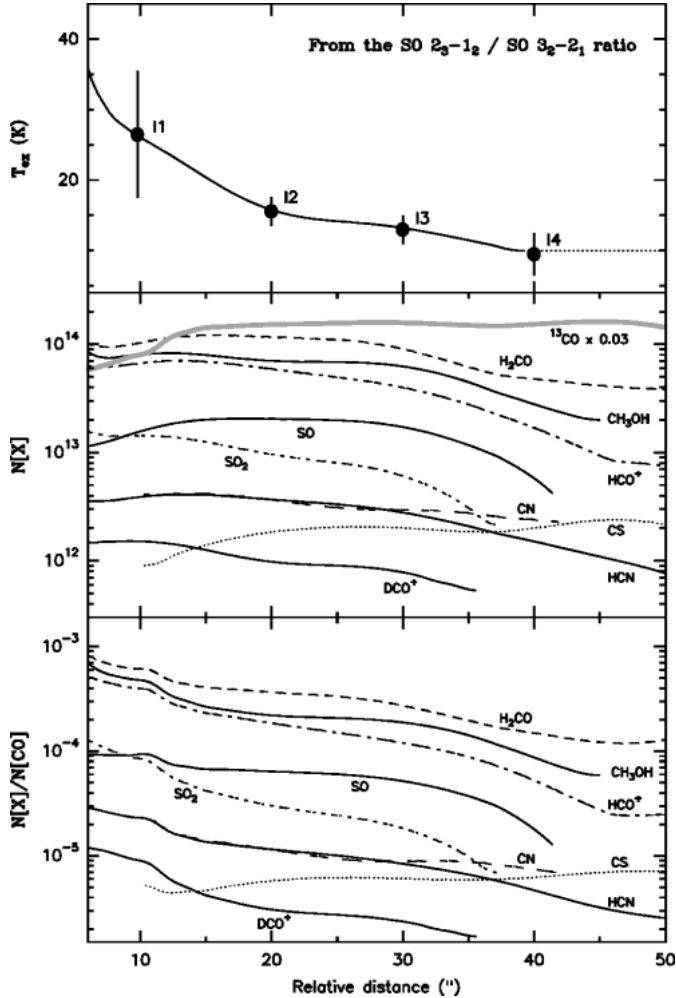


**Fig. 13.** Slices of the SO excitation temperature (top panel), column density (central panel) and relative abundance with respect to the CO (bottom panel) as a function of the distance to HH 2. The first position in the plot coincides with the position of the HH 2 knot E. The slice has 0 position  $\alpha(J2000) = 5^{\text{h}}36^{\text{m}}26^{\text{s}}.5$ ;  $\delta(J2000) = -6^{\circ}47'06''$ .0 and the position angle of the slice is  $\text{PA}=169^{\circ}$ . Note that the difference in column density with Figure 1 from Paper II are because in paper II we used a constant  $T_{\text{ex}}$  whereas in this paper we used the value derived from the SO line ratio. In the case of  $\text{HCO}^+$ , the new observations of  $\text{H}^{13}\text{CO}^+$  allowed to correct for optical depth.

density of the different molecular species assuming an excitation temperature equal to the SO excitation temperature. For  $\text{HCO}^+$ , its column density was corrected by taking into account  $\tau_{\text{HCO}^+}$  wherever  $\text{H}^{13}\text{CO}^+$  was detected, otherwise  $\tau_{\text{HCO}^+} = 6.0$  was adopted (which is the lowest  $\tau_{\text{HCO}^+}$  value measured in the slice). (3) The relative abundances with respect to CO.

Figure 13 shows the three parameters, SO excitation temperature, column density and abundance, along the slice. Table 4 gives the SO excitation temperature, column density at four positions along the slice, as well as the abundance increase factor at the first and last positions.

**Table 4.** Column densities for selected positions along the slice in the  $\text{SO}_2$  Clump

Position	I1	I2	I3	I4
$T_{\text{ex}}$ (K) <sup>a</sup>	$27 \pm 9$	$16 \pm 2$	$13 \pm 2$	$9 \pm 3$
$d_{\text{slice}}$ (") <sup>b</sup>	10	20	30	40
$d_{\text{HH2}}$ (") <sup>c</sup>	16	22	29	39

Molecule	$N[\text{mol}]$ ( $\text{cm}^{-2}$ )				$X_{\text{I1}}/X_{\text{I4}}$
CO	$1.7 \times 10^{17}$	$3.2 \times 10^{17}$	$3.3 \times 10^{17}$	$3.2 \times 10^{17}$	1
$\text{H}_2\text{CO}$	$1.0 \times 10^{14}$	$1.2 \times 10^{14}$	$9.0 \times 10^{13}$	$4.8 \times 10^{13}$	$4 \pm 1$
$\text{HCO}^+$	$6.7 \times 10^{13}$	$6.0 \times 10^{13}$	$4.0 \times 10^{13}$	$1.8 \times 10^{13}$	$8 \pm 1$
$\text{CH}_3\text{OH}$	$8.0 \times 10^{13}$	$7.1 \times 10^{13}$	$6.2 \times 10^{13}$	$2.8 \times 10^{13}$	$6 \pm 2$
SO	$1.6 \times 10^{13}$	$2.1 \times 10^{13}$	$1.7 \times 10^{13}$	$5.7 \times 10^{12}$	$5 \pm 1$
HCN	$3.9 \times 10^{12}$	$3.7 \times 10^{12}$	$2.8 \times 10^{12}$	$1.5 \times 10^{12}$	$5 \pm 1$
$\text{SO}_2$	$1.4 \times 10^{13}$	$9.7 \times 10^{12}$	$6.0 \times 10^{12}$	$< 2 \times 10^{12}$	$\gtrsim 12$
CS	$9.1 \times 10^{11}$	$1.8 \times 10^{12}$	$2.0 \times 10^{12}$	$2.0 \times 10^{12}$	$0.8 \pm 0.3$
CN	$4.1 \times 10^{12}$	$3.7 \times 10^{12}$	$3.0 \times 10^{12}$	$2.4 \times 10^{12}$	$3 \pm 2$
$\text{DCO}^+$	$1.5 \times 10^{12}$	$9.9 \times 10^{11}$	$7.8 \times 10^{11}$	$< 5 \times 10^{11}$	$\gtrsim 5$

<sup>a</sup> Error bars are at  $1-\sigma$

<sup>b</sup> Relative distance in the slice (see Fig. 13)

<sup>c</sup> Distance to HH 2 knot H

It is clear from this figure that the relative abundance enhancement towards HH 2 is observed in all molecular species except CS, which shows a relative abundance almost constant along the slice.  $\text{HCO}^+$  and  $\text{SO}_2$  are the species that have the highest enhancement.

In order to interpret the excitation temperature enhancement we used the RADEX package to fit the observed  $\text{SO } 3_2-2_1 / 2_3-1_2$  line ratios at the positions I1 ( $2.7 \pm 0.4$ ) and I3 ( $4.4 \pm 0.6$ ) given in Table 4. RADEX is a non-LTE molecular radiative transfer in an isothermal homogeneous medium (Schöier et al. 2005). In Figure 14 we show a set of the RADEX solutions in the  $T_{\text{kin}}-n(\text{H}_2)$  plane for the observed line ratios. The set of solutions in Fig. 14 that satisfy these averaged values indicates that the density in I1 ( $\gtrsim 10^6 \text{ cm}^{-3}$ ) is higher than in I3 ( $\sim 10^5 \text{ cm}^{-3}$ ), although the temperature cannot be constrained. Further observations of higher excitation lines at high angular resolution will help to better constrain the density enhancement and to determine the temperature.

#### 4.2. West Core

We first corrected the channel maps from the BIMA primary beam response and then convolved them with a Gaussian with a FWHM of  $30''$  in order to optimize the signal-to-noise ratio. The column densities were estimated from the resulting map at the position of the dust peak (see Figure 7) and for the  $v_{\text{LSR}}$  of  $6.3 \text{ km s}^{-1}$  component. Since we do not have information about the temperature of the molecular gas (no SO line is detected towards this core), we assumed an excitation temperature of 10 K. The narrow line widths of this velocity component indi-

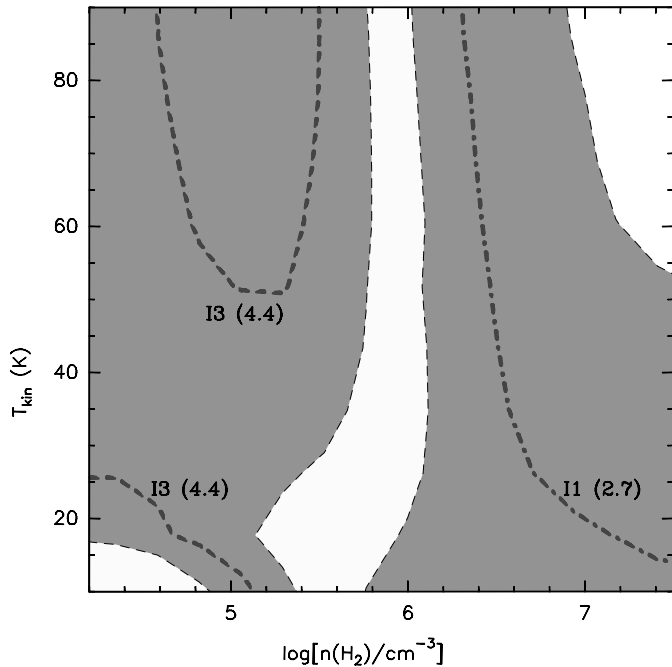


**Fig. 14.** Set of RADEX solutions in the  $T_{\text{kin}}-n(\text{H}_2)$  plane, for the observed SO  $3_2-2_1 / 2_3-1_2$  line intensity ratios (assuming a SO column density of  $2 \times 10^{14} \text{ cm}^{-2}$ ). The thick dashed lines is the contour for the ratio at position I3 (4.4) and the thick dotted-dashed line is the contour for the ratio at position I1 (2.7). The grey area shows the area within a  $\pm 1\sigma$ .

cate that the molecular gas is not shocked and, therefore, the temperature is probably low: even in the case that the West Core is in a similar situation as the SO<sub>2</sub> Clump (see § 5.3), the region with high temperatures would be probably compact. Fig. 2 of Dent et al. (2003) shows that the 850  $\mu\text{m}$  dust emission peak towards the West Core is  $\sim 90 \text{ mJy beam}^{-1}$ . Assuming that the dust temperature and opacity is similar to the Ahead Core, then the mean gas column density in the West Core at the dust peak is  $N(\text{H}_2) \simeq 1 \times 10^{22} \text{ cm}^{-2}$ . The beam averaged <sup>13</sup>CO column density at the dust peak and at an  $14''$  angular resolution (the same as the dust map) is  $2.8 \times 10^{15} \text{ cm}^{-2}$ , which gives an abundance of  $X[\text{CO}] \simeq 1.8 \times 10^{-5}$ . Table 5 shows the derived column densities and relative abundances for the  $30''$  smoothed spectra (adopting the aforementioned  $X[\text{CO}]$  value). From the <sup>13</sup>CO emission, we derive a mass of  $\sim 0.5 M_{\odot}$  for the West Core.

#### 4.3. The High Velocity Region

The column density for the HCO<sup>+</sup> and the upper limits (at  $3\sigma$ ) for the rest of the molecules were estimated at the intensity peak of the high velocity HCO<sup>+</sup> emission (see Fig. 9), which is  $\sim 3''$  northwest of the HH 2 knot E. The column densities are estimated from the integrated emission over the  $-5$  to  $5$  and  $11$  to  $21 \text{ km s}^{-1}$  velocity ranges, avoiding the contribution from the ambient gas of the Ahead Core (and the SO<sub>2</sub> Clump), and assuming an

**Table 5.** Column densities and abundances of the West Core

Molecule	$N[\text{mol}]$ ( $\text{cm}^{-2}$ )	$X[\text{mol}]/$ $X[\text{CO}]$	$X[\text{mol}]^a$
CO	$1.7 \times 10^{17}$	1.0	$1.8 \times 10^{-5}$
H <sub>2</sub> CO	$1.3 \times 10^{13}$	$8 \times 10^{-5}$	$1.4 \times 10^{-9}$
HCO <sup>+</sup>	$6.8 \times 10^{12}$	$4 \times 10^{-5}$	$7.2 \times 10^{-10}$
CH <sub>3</sub> OH	$\lesssim 2 \times 10^{13}$	$\lesssim 1 \times 10^{-4}$	$\lesssim 2 \times 10^{-9}$
SO	$\lesssim 2 \times 10^{12}$	$\lesssim 1 \times 10^{-5}$	$\lesssim 2 \times 10^{-10}$
HCN	$1.6 \times 10^{12}$	$9 \times 10^{-6}$	$1.7 \times 10^{-10}$
SO <sub>2</sub>	$\sim 2 \times 10^{12}$	$1 \times 10^{-5}$	$\sim 2 \times 10^{-10}$
CS	$1.6 \times 10^{12}$	$9 \times 10^{-6}$	$1.7 \times 10^{-10}$
CN	$3.3 \times 10^{12}$	$2 \times 10^{-5}$	$3.5 \times 10^{-10}$
DCO <sup>+</sup>	$\sim 2 \times 10^{11}$	$1 \times 10^{-6}$	$\sim 2 \times 10^{-11}$
C <sub>3</sub> H <sub>2</sub>	$\sim 7 \times 10^{11}$	$4 \times 10^{-6}$	$\sim 7 \times 10^{-11}$

<sup>a</sup>  $X[\text{mol}]$  is the abundance with respect to H<sub>2</sub>

**Table 6.** Column densities and abundances in the High Velocity Region

Molecule	$N(\text{mol})$ ( $\text{cm}^{-2}$ )	$N(\text{mol.})/N(\text{HCO}^+)$			
		HH 2	Shocked Regions <sup>a</sup>	Model A <sup>b</sup>	Model B <sup>b</sup>
HCO <sup>+</sup>	$4.1 \times 10^{13}$	1	1	1	1
CO	$< 1 \times 10^{17}$	$< 3000$	$2000-3 \times 10^5$	$2 \times 10^4$	$1 \times 10^4$
H <sub>2</sub> CO	$< 3 \times 10^{14}$	$< 8$	4–19	6.5	3.9
CH <sub>3</sub> OH	$< 3 \times 10^{14}$	$< 7$	70–2000	$2 \times 10^{-4}$	$4 \times 10^{-4}$
SO	$< 3 \times 10^{13}$	$< 0.7$	4–37	0.05	0.14
HCN	$< 4 \times 10^{12}$	$< 0.09$	2–18	200	500
SO <sub>2</sub>	$< 3 \times 10^{13}$	$< 0.8$	4–19	$3 \times 10^{-4}$	0.02
CS	$< 7 \times 10^{12}$	$< 0.2$	4–13	0.17	0.70
CN	$< 3 \times 10^{13}$	$< 0.7$	1.4–5	2.6	250
HC <sub>3</sub> N	$< 4 \times 10^{12}$	$< 0.1$	0.2–0.8	$4 \times 10^{-4}$	$9 \times 10^{-4}$
SiO	$< 4 \times 10^{12}$	$< 0.09$	0.6–40	...	...

<sup>a</sup> Range of values got from the molecular outflows in L1157 (Bachiller & Pérez Gutiérrez 1997), NGC 1333 IRAS2A (Jørgensen et al. 2004) and BHR71 (Garay et al. 1998)

<sup>b</sup> Theoretical ratios derived for shocked molecular gas under a strong UV fields: see more details in § 5.4

excitation temperature of 30 K. Table 6 shows the column densities and the relative abundances of several molecules with respect to HCO<sup>+</sup>, and for comparison we also give typical relative abundances in shocked regions of molecular outflows driven by low mass protostars. It is clear from this table that the HCO<sup>+</sup> abundance is strongly enhanced or, alternatively, that the other molecules are severely depleted in the High Velocity Region (see § 5.4).

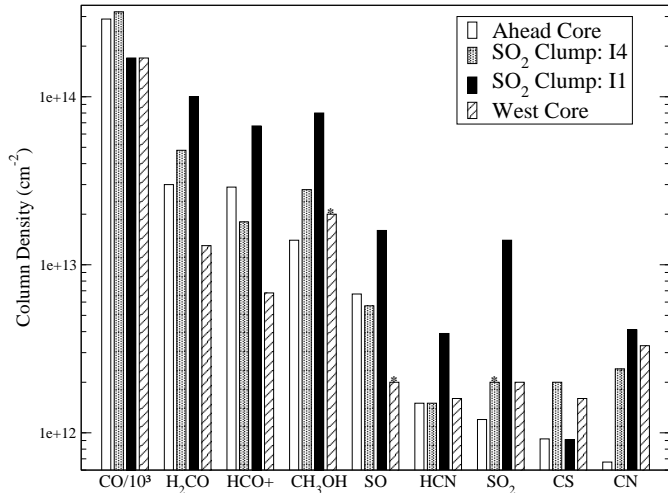


**Fig. 15.** Comparison of the column densities of several molecular species for the Ahead Core, the West Core and the positions I1 and I4 of the SO<sub>2</sub> clump. Position I1 is closer to HH 2 than I4 (see Fig. 13 and Table 4). Asterisks on the bar means upper limit of the column density.

## 5. Discussion

In this section, we attempt to provide possible explanations for the origin and structure of the observed molecular emissions in the frame of UV illumination models. We do not in any way attempt to model any of the regions in great detail. From now on we will define the SO<sub>2</sub> Clump as the molecular component within the Ahead Core traced by SO, SO<sub>2</sub> and CH<sub>3</sub>OH and whose chemical properties were studied in Papers I and II (see Fig. 2 from Paper I). The SO<sub>2</sub> Clump appears located in the region of the Ahead Core facing HH 2 (and thus is the molecular region in the Ahead Core more exposed to the UV radiation). Therefore, we split the discussion of the SO<sub>2</sub> Clump and Ahead Core in two different subsections. Figure 15 shows the column densities for the Ahead Core, SO<sub>2</sub> Clump and the West Core.

### 5.1. The SO<sub>2</sub> Clump

In § 4.1.3 we found an SO excitation temperature and relative molecular abundance enhancement within the SO<sub>2</sub> Clump towards HH 2 (see Figures 12 and 13). The excitation temperature enhancement indicates a density increase towards HH 2, which may suggest compression from the wind. Although the position at which the molecular enhancement occurs coincides very well with HH 2 knot E, the most likely source of UV radiation are the high excitation knots H and A (e. g., Böhm et al. 1992). This could be due to a projection effect: i. e., the molecular gas spatially coinciding with knot E could be the closest to knot H and A.

It is possible that the photoelectric heating mechanism due to the strong UV radiation could cause an increase in temperature in the molecular gas. We investi-

gated this scenario by running a PDR model that self-consistently computes the temperature at the edge of the clump (see Papadopoulos, Thi & Viti 2002 and Bell et al. 2005). We found that with a radiation field of  $\sim 40$  Habing (Molinari & Noriega-Crespo 2002; 1 Habing =  $1.6 \times 10^{-3}$  erg cm<sup>-2</sup> s<sup>-1</sup>) a temperature of 50 K is reached 1.0 mags into the clump for densities between  $10^5$  and  $10^6$  cm<sup>-3</sup>.

As already mentioned there is a definite gradient in both density and abundance. In light of this result, and recalling the conclusions of Paper II it is clear that the molecular enhancements found in the SO<sub>2</sub> Clump do *not* come from a single density component gas. We have therefore computed the observed column densities and the temperatures at four positions along the slice of Figure 13, see Table 4. In this table we also give the distance between the positions selected and the HH 2 knot H (which together with knot A are the likely source of the UV radiation). We then ran multi-density components models, using the chemical model employed in Paper II and revised visual extinctions. The physical and chemical parameters of these models were as those in B2 and in B7 in Paper II, but we used a number density structure with a minimum and maximum number density of respectively  $1 \times 10^5$  and  $3 \times 10^5$  cm<sup>-3</sup>. The maximum number density is as in B2 and B7 of Paper II, while the minimum density is determined by applying the density law derived by Tafalla et al. (2002) for starless cores. Since in our models the visual extinction is a function of the column density and therefore of the density, the visual extinction at any point in the modelled clump has changed from B2 and B7 accordingly.

We find that it is possible to match, within a factor of 5, all the species everywhere if the visual extinction (along the line of sight to the source) is  $\sim 3$  mags for all positions, and for ages  $< 1000$  yrs (*after* it starts being irradiated). Since we know the distance of the emitting region to the UV source ( $d_{HH2}$  in Table 4), a constant visual magnitude suggests one of the following three scenarios: (1) a decreasing (from HH 2) density structure with densities of  $1.4 \times 10^5$  cm<sup>-3</sup>,  $7.4 \times 10^4$  cm<sup>-3</sup>,  $5 \times 10^4$  cm<sup>-3</sup> and  $3.5 \times 10^4$  cm<sup>-3</sup> for positions I1, I2, I3 and I4, respectively (see Table 4); (2) a clumpy structure, where the density and size of each clump is constant (and hence the column density within each clump along the line of the source), and the difference in the observed column densities is simply due to the fact that as the radiation field crosses several clumps, it gets attenuated. This implies that the four positions correspond more or less to four clumps along the same line with respect to the source; (3) a third scenario may involve a more complicated picture where the line joining knots A, H and the SO<sub>2</sub> Clump is not perpendicular to the line of sight, hence the radiation field may be impinging on the SO<sub>2</sub> Clump from the top (or the bottom) along the line of sight to the observer. Probably the most likely scenario is a combination of the first and third scenarios. The first one agrees with the density increase towards HH 2 derived from the SO line ratios. The third one may agree with the distribution of the SO, SO<sub>2</sub> and CH<sub>3</sub>OH with respect to the dust: these molecules appear

located in the exposing face (with respect to HH 2) of the strongest 0.85 mm dust peak from the Ahead Core. In this case, the SO<sub>2</sub> Clump may not be a true clump, but just the illuminated face of a slightly larger clump, whose center is located at the position of the 0.85 mm dust peak.

On the basis of this model, we conclude that the HH 2 is the source of ‘illumination’ and that the SO<sub>2</sub> Clump must have substructure (a density increase towards HH 2, as a result of compression from the wind) within it (re-iterating a main conclusion of Paper II) and that this accounts for the chemical variation across the core. However, it is not possible to deduce from these studies whether the SO<sub>2</sub> Clump is a core distinct from the Ahead Core or is simply a face of Ahead Core strongly affected by the radiation from HH2.

## 5.2. The Ahead Core

The Ahead Core clearly shows some molecular abundance differences with respect to a typical starless dense core: for example, comparing the Ahead Core abundances with those from L1544 and L1689B (Jørgensen, Schöier, & van Dishoeck 2004), both CO and HCO<sup>+</sup> are slightly enhanced (a factor  $\sim 2$ –8), whereas the CS is depleted by a factor 9–26. We now explore whether, as for the SO<sub>2</sub> Clump, the abundances can be reproduced as a consequence of the UV field from the HH 2 shock impinging on the gas and dust of the core.

Excluding the SO<sub>2</sub> Clump, the Ahead Core has a large size,  $\sim 0.1$  pc, hence it is reasonable to assume that the species we are detecting may all be tracing different density components in this core. We used the models in Paper II to determine whether the chemistry of the core can be explained by a weak radiation field, because further away, that is impinging on a fairly dense core. We find that the results at early times ( $< 500$  yrs) of models from both Grid A and B from Paper II may match the observations fairly well (within a factor of 5, and with a radiation field of  $\sim 10$ –20 Habing) if one assumes that i) different densities along the line of the source are present and that ii) different molecules trace different components. For example, CS and CO emission seem to come mainly from the southern part of the Ahead Core, correlating well with a secondary dust peak, while HCN, H<sub>2</sub>CO and HCO<sup>+</sup> trace the whole core. These considerations suggest that the Ahead Core may not be an homogeneous and roughly spherical core but it may be composed of small clumps similar to those found in L673 (Morata, Girart & Estalella 2005). These BIMA observations reveal small-scale clumps (typically a few  $\times 10^{-2}$  pc) in lines of HCO<sup>+</sup>, N<sub>2</sub>H<sup>+</sup>, and CS. However, the maps of these species did not coincide; this is probably a consequence of the time-dependence of the chemistry (Garrod et al. 2005). A detailed modelling of this region, taking into considerations these assumption should be attempted.

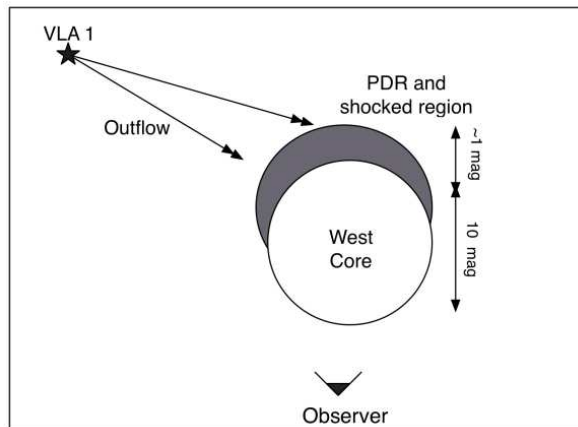


**Fig. 16.** Sketch of the West Core, the PDR-like structure, and shocked regions that lie behind the West Core with respect to the observer point of view.

## 5.3. The West Core

The well defined ring structure of optical and mid-IR emission (Warren-Smith & Scarrott 1999; Lefloch et al. 2005) around the West Core suggests that its geometry is quite spherical, with a radius of  $\sim 0.03$  pc. The size of the West Core is similar to those from the transient clumps resolved in L673 (Morata et al. 2005).

The presence of [SII] and H $\alpha$  in the ring indicates that the West Core is already being shocked by the protostellar winds of the YSO VLA 1. But how can the wind from VLA 1 form a ring structure around the West Core in the plane of the sky? A possible answer is that the shock comes from the ‘dark face’ of the West Core, as shown in the sketch of Figure 16. In this case, the cold and dynamically unperturbed molecular gas and dust is probably masking the shock where the column densities are high enough. The gas column density at the dust peak is  $N(\text{H}_2) \simeq 1 \times 10^{22} \text{ cm}^{-2}$  (see § 4.2), which implies a visual extinction of about 11 magnitudes. This is sufficient to create an apparent hole in the [SII] and H $\alpha$  emission at the center of the West Core. Following standard extinction laws (e.g., Mathis 1990), the mid-IR extinction ranges between  $\sim 0.2$  and  $0.7$  (i.e., an intensity decrease between 20% and 50%), which also can account for the observed mid-IR ring-like structures. The <sup>13</sup>CO, HCO<sup>+</sup>, HCN and CS spectra from the West Core show two lines, one at a  $v_{\text{LSR}}$  of  $\sim 6.3 \text{ km s}^{-1}$  and quite narrow (the FWHM of the <sup>13</sup>CO 1–0 line is  $\simeq 0.48 \pm 0.03 \text{ km s}^{-1}$ ), and a second line, weaker but broader,  $\Delta v \simeq 1.5 \text{ km s}^{-1}$ , centered at a  $v_{\text{LSR}}$  of  $\sim 8.7 \text{ km s}^{-1}$  (see Fig. 7). The narrow line possibly traces dynamically unperturbed molecular gas from the West Core, whereas the broader line may trace a molecular layer of interaction between the West Core and the shocked material. Further observations are required to confirm this hypothesis.

The ring-like mid-IR emission around the West Core is tracing warm gas interpreted by Lefloch et al. (2005) as a

PDR created by UV radiation field of 20–40 Habing. Thus, the properties of the West Core, i. e., an unperturbed dynamically core surrounded by PDR, suggest that the West Core is in a similar situation as the SO<sub>2</sub> Clump. However, the chemical composition of the West Core seems different: the column densities for most molecules are a factor of  $\sim 10$  lower in the West Core (Table 5) than in position I4 (Table 4), except for HCN, CS and CN which are of the same order.

The major constraints for the unperturbed cold molecular gas from a chemical point of view are that i) the line widths are narrow and hence the gas is probably not shocked; ii) there is an enhancement of HCO<sup>+</sup> with respect to a typical dense core *but* no other enhancement is observed and in fact CH<sub>3</sub>OH and SO are not even detected. The BIMA observations indicate a quiescent, possibly cold ( $< 30$ K) clump. On the other hand, Lefloch et al. (2005) detect warm gas interpreted as a PDR at the edge of this clump. We have run a PDR model (with a radiation field ranging from 20 to 40 Habing; Lefloch et al. 2005) of this region to estimate whether the presence of a PDR at the edge of the West Core can coexist with the quiescent dense gas we observe. We found that as long as the average density of the West Core is between  $5 \times 10^4$  and  $5 \times 10^5$  cm<sup>-3</sup>, then it is possible for the central region of the core to be cold. This range of densities are in agreement with those derived from the PDR (Lefloch et al. 2005). In particular we find that for a density of  $10^5$  cm<sup>-3</sup>, the gas temperature reaches 42 K at 1 mag and 27 K at 3 mags.

By combining the abundances of the modeled PDR with those from the models in Paper II we find that the best match is reached by a 2–component structure made of a fairly old quiescent, photo–processed clump ( $\sim 1000$  yrs of age) of thickness less than  $\sim 2$  mags plus a PDR component; such a combination gives the right abundances of CO, CS, H<sub>2</sub>CO and CH<sub>3</sub>OH (coming from the old dense clump), and of HCO<sup>+</sup> (coming mainly from the PDR); we find that the PDR needs to be at least 1 mag.

An alternative view is that the mid–IR emission comes not from a conventional PDR but from a warm interface with a PDR created in the interaction of the winds of the YSO VLA1 with the West Core. Nguyen, Hartquist & Williams (2001) have explored the physics and chemistry occurring in these interfaces, and have shown that the thermal pressures in the interfaces should significantly exceed those within the cloud. Resulting temperatures are expected to be  $\sim 10^3$  K and dust emissions may therefore mimic those of a PDR. The results of Nguyen et al. (2001) suggest that, if the interface occupies a few percent of the core, then some species may achieve detectable abundances. While CO and CS are not particularly enhanced above cold cloud abundances, in some conditions HCO<sup>+</sup> may be enhanced by up to two orders of magnitude above its cold cloud abundance. H<sub>2</sub>CO appears to be somewhat enhanced; results for methanol are not reported. Thus, it appears possible that the dynamical interaction of the wind and the clump may lead to a characteristic chem-

istry in the interface. Such a model requires more detailed study, perhaps along the lines of that by Lim, Rawlings & Williams (1999).

#### 5.4. The High Velocity Region

The properties of the high velocity HCO<sup>+</sup> emission associated with HH 2 are similar to those found in the NGC 2071 outflow (Girart et al. 1999): there is a good correlation with the shock–excited H<sub>2</sub> (see Fig. 8) and the emission has a monotonic enhancement with the flow velocity (Dent et al. 2003). The high velocity HCO<sup>+</sup> emission is also well correlated with optical knots with small proper motions (e. g., L, E), with (tangential) velocities in the 20–80 km s<sup>-1</sup> range (Bally et al. 2002). Since HCO<sup>+</sup> is expected to be strongly enhanced in turbulent mixing layers associated with low–velocity (40 km s<sup>-1</sup>) shocks (Taylor & Raga 1995), Dent et al. (2003) suggested that this flow velocity enhancement dependence could be explained if the HCO<sup>+</sup> is formed at high shock velocities and then gradually mixes with ambient unenhanced material. This is like the wake chemistry explored by Lim et al. (1999) and implies that a UV radiation may not be necessary in the chemical processing of the HCO<sup>+</sup> (Dent et al. 2003). However, in the mixing layer scenario one would expect other molecules, such as CS, H<sub>2</sub>CO, SO, to be also enhanced (e. g., Viti, Natarayan & Williams 2002), but these are undetected in the High Velocity Region.

Analysis from the mid–IR H<sub>2</sub> line emission shows that the 0–0 S(*n*) lines have contributions from hot ( $\sim 1000$  K) and warm ( $\sim 300$  K) components (Lefloch et al. 2003). The hot component arises from compact regions ( $\lesssim 2''$ ), with shock velocities of 20–30 km s<sup>-1</sup>. The warm component arises from more extended and slower shocks (10–15 km s<sup>-1</sup>) in a denser medium,  $\sim 10^5$  cm<sup>-3</sup>. The fact that the high velocity HCO<sup>+</sup> emission is better correlated with the S(2) H<sub>2</sub> line than with higher excitation H<sub>2</sub> lines and that this line traces the warm H<sub>2</sub> component suggest that the high velocity HCO<sup>+</sup> probably arises from or around the H<sub>2</sub> warm component.

As for the other three regions, we have attempted to qualitatively model the high velocity gas. The chemical anomaly of this gas is that it differs substantially from a typical shocked region (see Table 6). In addition, we have tried to see whether UV radiation alone can reproduce the HCO<sup>+</sup> overabundance and found that this is not the case. We have investigated whether it is possible, via a combination of heating (e.g. induced by the passage of a low velocity, non-dissociative shock, as the HCO<sup>+</sup> and warm H<sub>2</sub> correlation suggests) and UV chemistry, for a gas to have such a composition as we find here, i.e. abundant HCO<sup>+</sup> without the presence of other shock tracers such as SiO and CH<sub>3</sub>OH.

The models used for this region are similar to those employed in Viti et al. (2004) where we explore the chemical evolution of low velocity, chemically rich clumps observed along the main axis of chemically rich outflows. The

chemical model simulates the clump formation (by free-fall collapse) and its subsequent interaction with the outflow; here we only consider the scenario where the density structure formed before the advent of the outflow (see Viti et al. 2004 for a more detailed explanation of the model). In addition, here we also include the presence of a strong radiation field. After a first stage where densities of up to  $10^5 \text{ cm}^{-3}$  are reached, the region is heated and affected by a very strong UV field. We simulate a short period ( $\sim 100$  yrs) of high temperature ( $\sim 1000$  K), followed by cooling, down to a temperature of 200 K. We employ a UV field of 100 Habing; this value is derived from the consideration that if the edge of the West Core is affected by a UV field of 20–40 Habing, then since the High Velocity Region is closer to the HH shock by a factor two the radiation field impinging on it should be about four times stronger. Table 6 reports the column densities computed for species observed in this shocked gas. Observations show that the only detected molecule is  $\text{HCO}^+$  while for the other species we have upper limits. We tested two models: Model A where we assumed a core size of  $\sim 0.02$  pc that, at a density of  $10^5 \text{ cm}^{-3}$ , corresponds to a visual magnitude of  $\sim 4.8$  mags; and Model B, as Model A but for a smaller clump of 0.01 pc, corresponding to a visual magnitude of 2.8 mags. We ran the chemistry for 100,000 yrs.

For model A we found that the best match with observations is reached at 40,000 yrs, where  $\text{HCO}^+$  peaks with a fractional abundance of  $5 \times 10^{-9}$ ; the gas has by then completely cooled down (to 200 K). For model B we found that  $\text{HCO}^+$  peaks earlier, at 1000 yrs; the  $\text{HCO}^+$  fractional abundance is  $6 \times 10^{-9}$ . For both models, we report in Table 6 the ratios for selected species to be compared with those observed and shown in the same table. If we consider that the HH jet is traveling at velocities of hundreds of  $\text{km s}^{-1}$ , then model B seems more realistic because of the shorter timescales involved.

There is a remarkable correspondence between the computed peak abundance of  $\text{HCO}^+$ , and the observed column density: the latter is derived from observations to be  $4.1 \times 10^{13} \text{ cm}^{-2}$  which implies that for a 0.01 pc clump (Models B) the observed fractional abundance is  $\sim 8.9 \times 10^{-9}$ .

In model B,  $\text{HCO}^+$  reaches  $\sim 10^{-9}$  very early, at about 500 years; it then increases but after about 1500 yrs starts being destroyed (a consequence of the lower  $A_V$ ). However, during these 1000 yrs, which include the cooled phase,  $\text{HCO}^+$  is  $\sim 5 \times 10^{-9}$  for about 400 yrs and during that period the ratios of most of the other species to  $\text{HCO}^+$  are consistent with the observed ratios ( $\text{CO}/\text{HCO}^+$  is higher than the ratio estimated from the observations by Dent et al. 2003). In Table 6 we report theoretical ratios for all the species, (but not for  $\text{SiO}$ , which is not included in our models), for which either a detection or an upper limit is derived from observations. We chose to show the ratios at the time when  $\text{HCO}^+$  peaks in our models. The species that differ most from observations are HCN and CN. As extensively explained in Paper II, there is a funda-

mental problem with these two species that at the moment we are unable to explain.

In summary, we have found two suitable scenarios that match the observations of the High Velocity Region except for the CO, CN, and HCN abundances. The essential feature is of a warm chemistry (possibly due to the passage of a low velocity, non-dissociative shock) which is subjected to stronger than ambient UV field, a scenario not previously explored.

### 5.5. Is the molecular gas ahead of HH 2 being driven out by the VLA 1 winds?

The kinematical properties described in § 3.4 suggest that the Ahead Core is being driven by the protostellar winds from VLA 1. If the velocity gradient observed is due to the swept-up effect from the winds, then these winds should have a low collimation since the dense molecular structure traced by the  $\text{HCO}^+$  (including the Ahead Core) is quite extended. Low collimated winds sweeping up dense molecular gas have been observed around the HH 34 system (Anglada et al. 1995) and XZ Tauri (Welch et al. 2000).

We considered a model of a spherically symmetric stellar wind, with constant velocity  $V_w$  and mass-loss rate  $\dot{M}_w$ , sweeping up the ambient material as a snow-plow and accumulating it into a shell. Anglada et al. (1995) obtains analytical solutions in the case of non-negligible ambient cloud pressure  $\rho \Delta V_c^2$ , for ambient cloud density power-law distributions,  $\rho \propto r^{-\alpha}$ , with  $\alpha = 2$  and  $\alpha = 0$  (constant density).  $\Delta V_c$  is the mean squared velocity (turbulent plus thermal) in the ambient cloud. The parameters of the shell used were those observed for the Ahead Core,  $R_{\text{shell}} = 5 \times 10^4$  AU, the distance from the Ahead Core to VLA 1,  $V_{\text{shell}} = 3.0 \text{ km s}^{-1}$ , the maximum velocity relative to the systemic velocity observed in the Ahead Core, and  $M_{\text{shell}} = 3.8 M_{\odot}$ , the mass derived from the dust (Dent et al. 2003), and a mean-squared velocity  $\Delta V_c = 0.6 \text{ km s}^{-1}$ , the typical observed line width. Table 7 shows the physical parameters obtained for the density of the ambient cloud, the age of the shell, the momentum rate of the stellar wind, and the mass-loss rate for a wind velocity of  $100 \text{ km s}^{-1}$ .

In our case we are only observing the southern part of the region surrounding the powering source of the HH 1–2 outflow, VLA 1, and the Ahead Core subtends only a small solid angle  $\Omega < 4\pi$  sr around VLA 1. However, the results obtained for a spherically symmetric wind are applicable to the case of a conical stellar wind. In general, if the solid angle of the wind cone  $\Omega_w$  is greater than the shell solid angle  $\Omega_{\text{shell}}$ , the momentum rate, and mass-loss rate obtained in the spherically symmetric case have to be increased by a factor  $\Omega_w/\Omega_{\text{shell}}$ .  $\Omega_w$  is at least 4 times the observed  $\Omega_{\text{shell}}$ ; a factor of 2 comes from the fact that the wind is bipolar, and an additional factor of 2 comes from the fact that the outflow axis is very close to the plane of the sky (Solf & Bohm 1991) and that the Ahead

**Table 7.** Physics of the wind driven Ahead Core<sup>a</sup>

Parameter	Value	
$\alpha^b$	0	2
$t_{\text{shell}}$ (yr)	$3.9 \times 10^4$	$7.9 \times 10^4$
$n(\text{H}_2)$ ( $\text{cm}^{-3}$ )	$1.3 \times 10^3$	$4.3 \times 10^2$ <sup>c</sup>
$\dot{P}_w$ ( $M_\odot \text{ yr}^{-1} \text{ km s}^{-1}$ )	$2.9 \times 10^{-4}$	$1.5 \times 10^{-4}$
$\dot{M}_w^d$ ( $M_\odot \text{ yr}^{-1}$ )	$2.9 \times 10^{-6}$	$1.5 \times 10^{-6}$

<sup>a</sup> Obtained for shell parameters  $R_{\text{shell}} = 5 \times 10^4$  AU,  $V_{\text{shell}} = 3.0 \text{ km s}^{-1}$ ,  $M_{\text{shell}} = 3.8 M_\odot$ , and  $\Delta V_c = 0.6 \text{ km s}^{-1}$ .

<sup>b</sup> Power index of the the radial density distribution,  $n(\text{H}_2) \propto r^{-\alpha}$

<sup>c</sup> Value for a distance of  $5 \times 10^4$  AU.

<sup>d</sup> Value obtained assuming a wind velocity of  $100 \text{ km s}^{-1}$ .

Core lies in the foreground face of the outflow lobe (see § 3.4), and, for symmetry, the wind has to exist also in the background face. In conclusion, the density, momentum rate, and mass-loss rate obtained in Table 7 should be at least a factor of  $\sim 4$  higher.

As the outflow axis lies near the plane of the sky, projection effects have to be accounted for. The de-projected velocity and distance are  $V_{\text{shell}}/\sin i$  and  $R_{\text{shell}}/\cos i$ , respectively, where  $i$  is the inclination with respect to the plane of the sky. However, the inclination is the biggest uncertainty. The dynamical age of the HH 1–2 outflow,  $\sim 1 \times 10^4$  yr ago (Ogura 1995) and the momentum rate of the HH 1–2 jet is  $8 \times 10^{-4} M_\odot \text{ yr}^{-1} \text{ km s}^{-1}$  (Chernin & Masson 1995). Given the uncertainties, the wind driven model can roughly account for these values for inclinations in the range  $30^\circ$ – $45^\circ$ . For such a range  $t_{\text{shell}}$  does not change much (a factor 0.6–1) and the outflow momentum rate (for  $\alpha = 2$ ) becomes  $\sim 1$ – $2 \times 10^{-3} M_\odot \text{ yr}^{-1} \text{ km s}^{-1}$ .

The total mass of the molecular gas and dust in the HH 1–2 region, derived from ammonia observations, is  $\sim 52 M_\odot$  (Torrelles et al. 1994). Taking into account the mass of Ahead Core and of the West Core ( $\sim 4.1 M_\odot$ ), the fraction of the molecular mass that is being driven out by the VLA 1 winds in the HH 2 lobe is  $\sim 8\%$ . Since it is possible that a similar situation may happen in the northern lobe around HH 1 (Torrelles et al. 1993 found also ‘quiescent’ ammonia clumps ahead of HH 1) the total mass driven by the powerful VLA 1 is likely 10–15 % of the total mass in the HH 1–2 region.

Finally, it is interesting that while the molecular abundances may be explained by chemical models of pre-existing quiescent and transient clumps irradiated by a strong UV field (see previous sections and Paper II), the kinematics of the regions suggests that the molecular gas is indeed driven out by protostellar winds and the SO line ratios in the SO<sub>2</sub> clump indicate a density increase towards HH 2. These results seem to be apparently in contradiction. Although beyond the scope of this paper and possi-

bly quite speculative, it is possible that these clumps have formed due compression by winds but in a somewhat similar way (though probably faster) to the formation of the transient clumps. The presence of transient clumps within molecular clouds has been reported recently both observationally (Morata et al. 2005) and theoretically (e. g., Falle & Hartquist 2002; Vázquez-Semadeni et al. 2005).

## 6. Summary and Conclusions

We have carried out an extensive observational study (from BIMA data) and attempted a preliminary theoretical investigation of the molecular gas around HH 2. The BIMA maps show a very complex morphological, kinematical and chemical structure of the molecular gas. For clarity we divided the observed region in four subregions taking into account the properties of the different molecular species and the properties observed at other wavelengths:

- The Ahead Core, located ahead of HH 2, which has a size of  $\sim 0.1$  pc and a mass of  $3.8 M_\odot$  (Dent et al. 2003). The observed molecular abundances from the Ahead Core differ from the typical values of low-mass protostellar envelopes. A weak UV field (weak because attenuated when passing through the SO<sub>2</sub> clump) originated in HH 2 can account for the observed values if different species trace different layers. The differences between species within the Ahead Core suggest that it is not homogeneous but probably composed by small clumps.

- The SO<sub>2</sub> Clump is a molecular component within the Ahead Core that is more exposed to the UV radiation from HH 2. The analysis of the observed molecular lines indicates an increase of density and relative molecular abundances towards HH 2. The photoelectric heating produced by the strong UV field could probably create a temperature enhancement at the edge of the clump. A four point chemical analysis of the SO<sub>2</sub> Clump confirms the conclusion of Paper II that the clump must have substructure within it if its chemistry is due to the HH 2 UV illumination. In particular, an increase of density towards HH 2 may account for the chemical properties, which would suggest compression from the VLA 1 winds. From the overall properties of the SO<sub>2</sub> Clump we cannot say whether it is a clump distinct from the Ahead Core, or, whether it is part of the face of the Ahead Core exposed to HH 2.

- The West Core is a molecular structure with a radius of  $0.03$  pc and a mass of  $\sim 0.3 M_\odot$  surrounded by a ring structure of shocked gas traced by [SII] and H $\alpha$  (Warren-Smith & Scarrott 1999) and of a PDR-like structure traced by mid-IR hot dust and PAH emission (Lefloch et al. 2005). This ring-like structure is likely not real but a consequence of the fact that the West Core is in the foreground with respect to the shocked and hot component. The properties of the West Core and the SO<sub>2</sub> Clump are somewhat similar



(i. e., apparently quiescent gas irradiated by a strong UV field), although their chemistry is different. We find that the chemistry of the West Core can be best explained as arising from a combination of an old photo-processed dense clump, responsible for the emission of CO, CS, H<sub>2</sub>CO and CH<sub>3</sub>OH, and a PDR, from where most HCO<sup>+</sup> emission comes. Alternatively, the mid-IR emission may not come from a conventional PDR but from a warm interface with PDR created in the interaction of the VLA 1 outflow with the West Core, which may also account for the HCO<sup>+</sup> emission.

- The High Velocity Region, associated with HH 2, is traced by the HCO<sup>+</sup> but not by other molecular shock tracers such as SiO, CS and CH<sub>3</sub>OH. The presence of enhanced HCO<sup>+</sup> and the lack of other shock tracers can be accounted by the interaction of the VLA 1 outflow with a pre-existing dense clump *via* heating (possibly due to the passage of a low velocity, non-dissociative shock) and by the presence of strong UV field (coming from the nearby high excitation HH 2 knots), although our models predict excessive abundances of HCN and CN.

The overall main conclusion of this work confirms the findings of Paper I and II, by demonstrating that in addition to the strong photochemical effects caused by penetration of the UV photons from HH 2 into molecular cloud, a range of complex radiative and dynamical interactions occur. These generate characteristic chemical signatures for each type of interaction. Thus, despite the apparent ‘quiescent’ nature of the molecular cloud ahead of HH 2, the kinematical properties observed within the field of view suggest that the cloud is not ‘quiescent’ but it is possibly being driven out by the powerful winds from the VLA 1 protostar. If so, this would imply that a significant fraction (10–15 %) of the total mass in the HH 1–2 region is being disrupted from the original molecular dense core around the protostar. Given the large size of the molecular emission, these winds should be of lower collimation than the jet associated and responsible of HH 1 and 2.

*Acknowledgements.* We thank J. M. Torrelles and S. Curiel for providing the NH<sub>3</sub> and [SII] images, respectively. We thank the anonymous referee for the thorough review of the paper. JMG was supported by RED–2000 from the Generalitat de Catalunya. JMG and RE are partially supported by SEUI grant AYA2002-00205. SV acknowledges individual financial support from a PPARC Advanced Fellowship. DAW thanks the Leverhulme Trust for the award of an Emeritus Fellowship.

## References

- Amin, M. Y. 2001, *New Astronomy*, 6, 393  
 André, P., Ward-Thompson, D., & Barsony, M. 2000, *Protostars and Planets IV*, 59  
 Anglada, G., Estalella, R., Mauersberger, R., et al. 1995, *ApJ*, 443, 682  
 Bachiller, R., & Pérez Gutiérrez, M. 1997, *ApJ*, 487, L93  
 Bally, J., Heathcote, S., Reipurth, B., et al. 2002, *AJ*, 123, 2627  
 Bell, T. A., Viti S., Williams, D. A., Crawford I. A., & Price, R. J. 2005, *MNRAS*, 357, 961  
 Böhm, K. H. & Solf, J. 1992, *AJ*, 104, 1193  
 Chernin, L. M. & Masson, C. R. 1995, *ApJ*, 443, 181  
 Choi, M., & Zhou, S. 1997, *ApJ*, 477, 754  
 Davis, C. J., Dent, W. R. F., & Bell Burnell, S. J. 1990, *MNRAS*, 244, 173  
 Dent, W. R. F., Furuya, R. S., & Davis, C. J. 2003, *MNRAS*, 339, 633  
 Falle, S. A. E. G., & Hartquist, T. W. 2002, *MNRAS*, 329, 195  
 Flower, D. R., Pineau des Forets, G., Field, D., & May, P. W. 1996, *MNRAS*, 280, 447  
 Garay, G., Köhnenkamp, I., Bourke, T. L., Rodríguez, L. F., & Lehtinen, K. K. 1998, *ApJ*, 509, 768  
 Garrod, R. T., Williams, D. A., Hartquist, T. W., Rawlings, J. M. C., & Viti, S. 2005, *MNRAS*, 356, 654  
 Girart, J. M., Ho, P. T. P., Rudolph, A. L., et al. 1999, *ApJ*, 522, 921  
 Girart, J. M., Rodríguez, L. F., Anglada, G., et al. 1994, *ApJ*, 435, L145  
 Girart, J. M., Viti, S., Williams, D. A., Estalella, R., & Ho, P. T. P. 2002, *A&A*, 388, 1004 (Paper I)  
 Hester, J. J., Stapelfeldt, K. R., & Scowen, P. A. 1998, *AJ*, 116, 372  
 Jørgensen, J. K., Schöier, F. L., & van Dishoeck, E. F. 2004, *A&A*, 416, 603  
 Jørgensen, J. K., Hogerheijde, M. R., Blake, G. A., et al. 2004, *A&A*, 415, 1021  
 Langer, W. D., & Penzias, A. A. 1993, *ApJ*, 408, 539  
 Lefloch, B., Cernicharo, J., Cabrit, S., et al. 2003, *ApJ*, 590, L41  
 Lefloch, B., Cernicharo, J., Cabrit, S., & Cesarsky, D. 2005, *A&A*, 433, 217  
 Lim, A. J., Rawlings J. M. C., Williams D. A. 1999, *A&A*, 308, 1126  
 Mathis, J. S. 1990, *ARA&A*, 28, 37  
 Molinari, S., & Noriega-Crespo, A. 2002, *AJ*, 123, 2010  
 Morata, O., Girart, J.M., Estalella, R. 2005, *A&A*, in press  
 Moro-Martín, A., Cernicharo, J., Noriega-Crespo, A., & Martín-Pintado, J. 1999, *ApJ*, 520, L111  
 Nguyen T. K., Hartquist T. W., Williams D. A. 2001, *A&A*, 366, 662  
 Ogura, K. 1995, *ApJ*, 450, L23  
 Papadopoulos P. P., Thi W.-F., & Viti S. 2002, *ApJ*, 579, 270  
 Pravdo, S. H., Fegelson, E. D., Garmire, G., et al. 2001, *Science*, 413, 708  
 Raymond, J. C., Blair, W. P., & Long, K. S. 1997, *ApJ*, 489, 314  
 Richer, J. S., Shepherd, D. S., Cabrit, S., Bachiller, R., & Churchwell, E. 2000, *Protostars and Planets IV*, 867  
 Schöier, F. L., van der Tak, F. F. S., van Dishoeck, E. F., & Black, J. H. 2005, *A&A*, 432, 369  
 Solf, J. & Bohm, K. H. 1991, *ApJ*, 365, 618  
 Tafalla, M., Myers, P. C., Caselli, P., Walmsley, C. M., & Comito, C. 2002, *ApJ*, 569, 815  
 Taylor, S.D., & Raga, A. 1995, *A&A*, 296, 823  
 Taylor, S. D., & Williams, D. A. 1996, *MNRAS*, 282, 1343  
 Torrelles, J. M., Rodríguez, L. F., Canto, J., et al. 1992, *ApJ*, 396, L95  
 Torrelles, J. M., Gomez, J. F., Ho, P. T. P., et al. 1993, *ApJ*, 417, 655  
 Torrelles, J. M., Gomez, J. F., Ho, P. T. P., et al. 1994, *ApJ*, 435, 290

- Vázquez-Semadeni, E., Kim, J., Shadmehri, M., & Ballesteros-Paredes, J. 2005. *ApJ*, 618, 344
- Viti, S. & Williams, D. A. 1999, *MNRAS*, 310, 517
- Viti, S., Natarayan, S. & Williams, D. A. 2002, *MNRAS*, 336, 797
- Viti, S., Girart, J. M., Garrod, R., Williams, D. A., & Estalella, R. 2003, *A&A*, 399, 187 (Paper II)
- Viti, S., Codella, C., Benedettini, M., & Bachiller, R. 2004, *MNRAS*, 350, 1029
- Warren-Smith, R. F. & Scarrott, S. M. 1999, *MNRAS*, 305, 875
- Welch, W. J., Hartmann, L., Helfer, T., & Briceño, C. 2000, *ApJ*, 540, 362

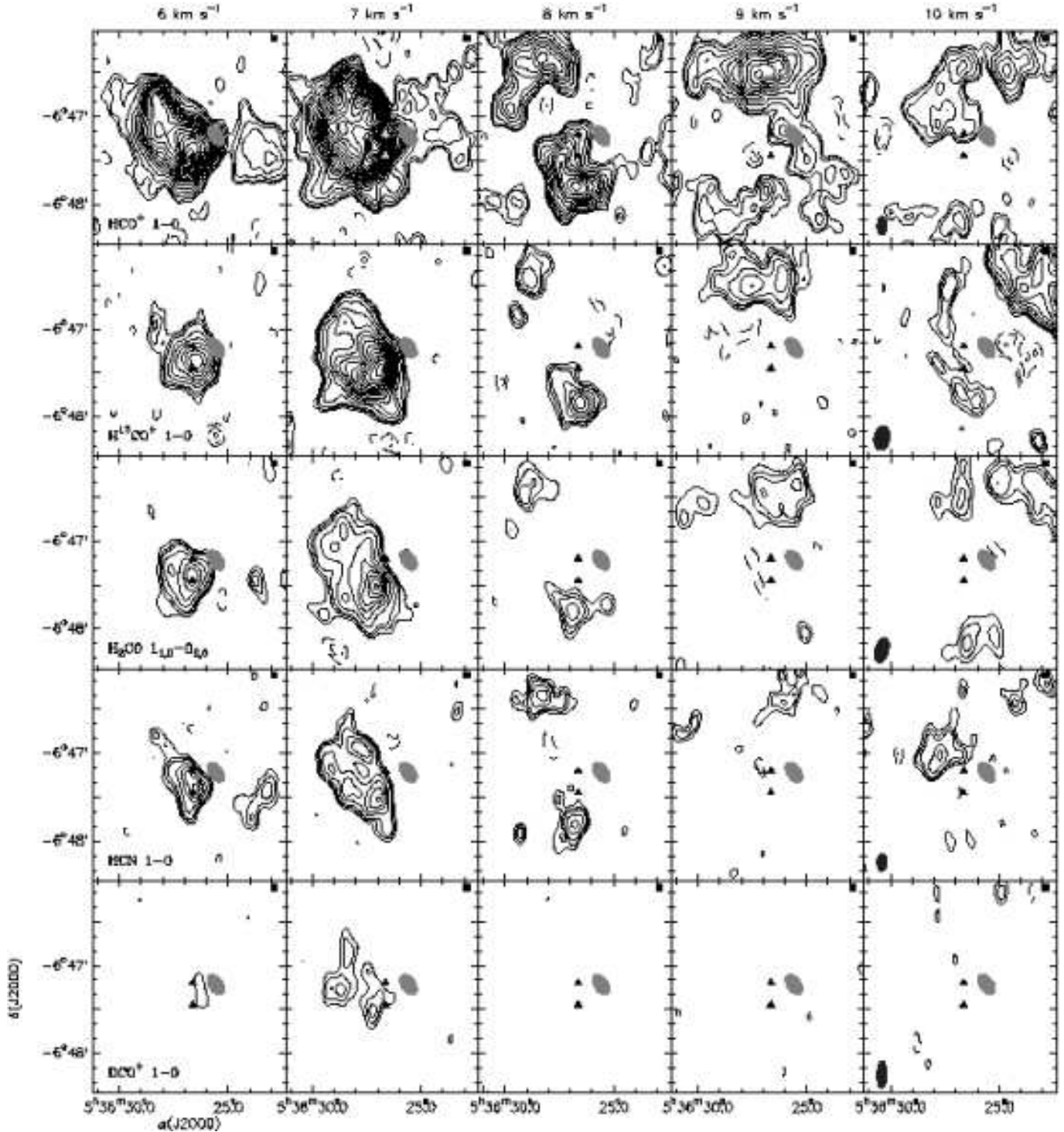


**Fig. 1.** Channel velocity (for  $\Delta v = 1 \text{ km s}^{-1}$ ) BIMA contour maps of  $\text{HCO}^+$ ,  $\text{H}^{13}\text{CO}^+$ ,  $\text{H}_2\text{CO}$ ,  $\text{HCN}$  and  $\text{DCO}^+$  (the maps are not corrected for primary beam attenuation). For the  $\text{HCO}^+$  the contours are -4, -3, 3, 4, 6, 9, 12, 15, 18, 21, 24, 27, 30, ... 80 times the *rms* noise of the map,  $62 \text{ mJy beam}^{-1}$ . Contours are -4, -3, 3, 4, 5, 7, 9, 11, ... 31 times the *rms* noise of the maps: 55 ( $\text{H}^{13}\text{CO}^+$ ), 120 ( $\text{H}_2\text{CO}$ ), 36 ( $\text{HCN}$ ), and 140  $\text{mJy beam}^{-1}$  ( $\text{DCO}^+$ ). The CN  $N=1-0$  map was obtained by combining the following hyperfine transitions:  $F=5/2-3/2$ ,  $J=3/2-1/2$   $F=3/2-1/2$  and  $J=1/2-1/2$   $F=3/2-3/2$  (note that Table 2 give the *rms* of the maps previous to this combination procedure). The synthesized beam is shown in the lower left corner of the right panels. The grey ellipsoid shows the position of the brightest HH 2 knots (A, B, D, H). The two filled triangles show the position of HH 2 knots E (northern one) and L (southern one). The filled square shows the position of the driving source of HH 2.

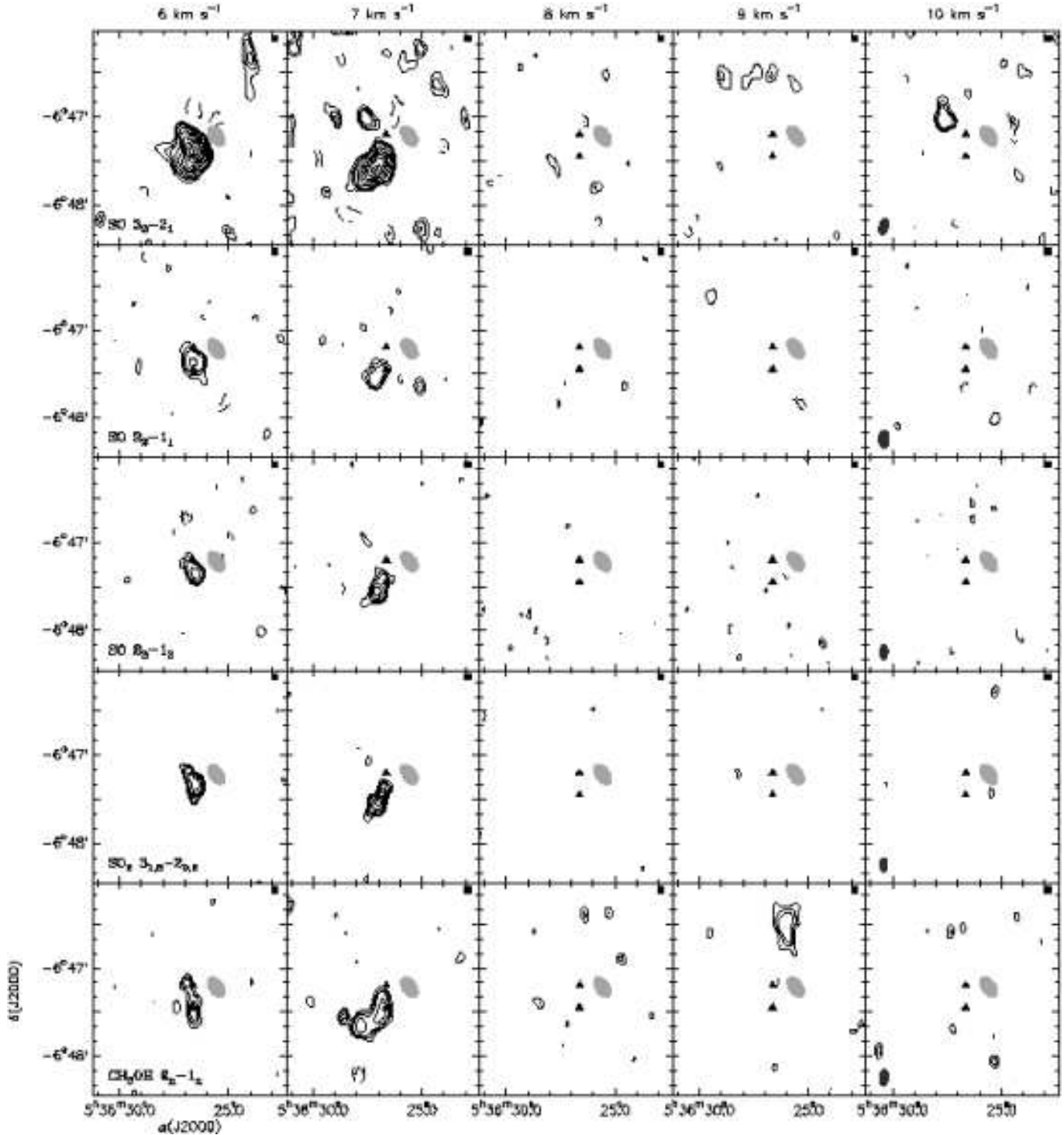


**Fig. 2.** Channel velocity BIMA contour maps of three SO lines, SO<sub>2</sub> and CH<sub>3</sub>OH (the maps are not corrected for primary beam attenuation). Contours are -4, -3, 3, 4, 5, 7, 9, 11, ... 25 times the *rms* noise of the maps: 95 (SO 3<sub>2</sub>-2<sub>1</sub>), 85 (SO 2<sub>2</sub>-1<sub>1</sub>), 73 (SO 2<sub>3</sub>-1<sub>2</sub>), 33 (SO<sub>2</sub>), and 50 mJy beam<sup>-1</sup> (CH<sub>3</sub>OH). The CH<sub>3</sub>OH map was obtained by combining the 2<sub>0</sub>-1<sub>0</sub>A<sup>+</sup> and 2<sub>-1</sub>-1<sub>-1</sub> E transitions (note that Table 2 give the *rms* of the maps previous to this combination procedure).

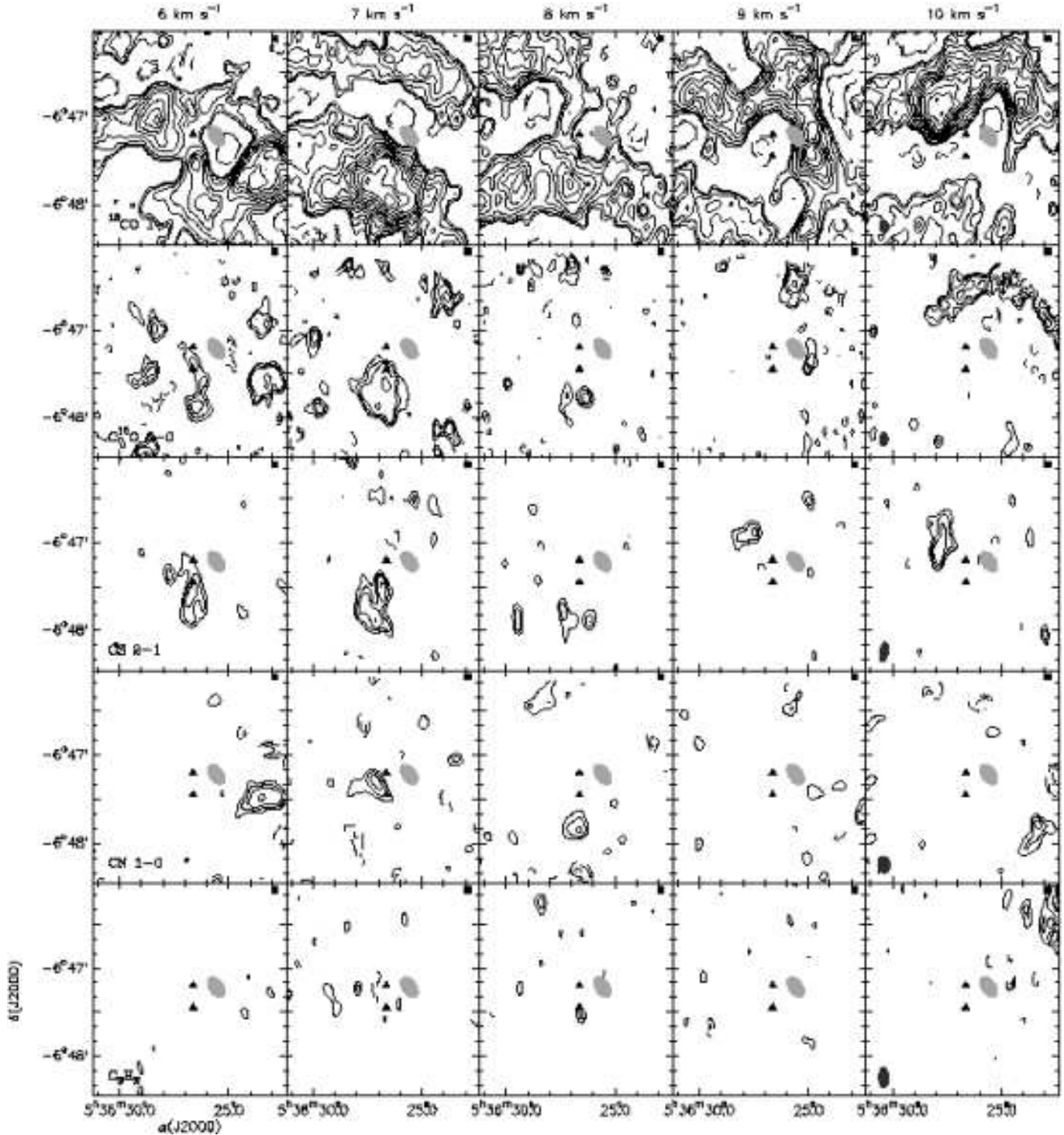


**Fig. 3.** Channel velocity BIMA contour maps of  $^{13}\text{CO}$ ,  $\text{C}^{18}\text{O}$ , CS, CN and  $\text{C}_3\text{H}_2$  (the maps are not corrected for primary beam attenuation, except for  $^{13}\text{CO}$ ). Contours are -4, -3, 3, 4, 5, 7, 9, 11, ... 25 times the *rms* noise of the maps: 85 ( $^{13}\text{CO}$ ), 75 ( $\text{C}^{18}\text{O}$ ), 83 (CS), 50 (CN), and 52  $\text{mJy beam}^{-1}$  ( $\text{C}_3\text{H}_2$ ). The HCN  $J=1-0$  map was obtained by combining the three hyperfine transitions:  $F=2-1$ ,  $F=1-1$  and  $F=0-1$  (note that Table 2 give the *rms* of the maps previous to this combination procedure). The  $\text{C}^{18}\text{O}$  1-0 maps were obtained combing 109.7–113.0 and 109.9–113.4 GHz (LSB–USB) frequency setups.